

Model-Based Tensor Decompositions for Geophysical Parameter Retrieval From Multidimensional SAR Data

Nikita Basargin¹, Graduate Student Member, IEEE, Alberto Alonso-González²,
and Irena Hajnsek³, Fellow, IEEE

Abstract—Tensor decompositions are mathematical methods for joint analysis and information extraction from multidimensional data. This work combines model-free algebraic tensor decompositions with physical synthetic aperture radar (SAR) models and introduces a novel framework for geophysical parameter retrieval from multidimensional SAR tensors. To demonstrate parameter retrieval, we combine information from polarimetric, temporal, and spatial data dimensions and invert soil moisture over vegetated agricultural areas. We formulate parameter inversion as a constrained optimization problem and retrieve the parameters by fitting the physical model to the observed SAR tensor. Compared to methods that operate on matrices, multidimensional tensors offer a larger observation space, reduce inversion ambiguities, and allow inversion of more complex models that cover a larger range of field conditions and crop types. The proposed method represents the signal as a sum of three components, separates the surface, dihedral, and volume signal contributions, and allows estimation of crop-specific volume scattering polarimetric signatures. With the increasing availability of multidimensional SAR data, model-based tensor decompositions gain relevance and provide a flexible, extensible, and explainable way to jointly analyze the information across multiple data dimensions.

Index Terms—Optimization, physical models, polarimetry, soil moisture, synthetic aperture radar (SAR), tensor decompositions, time series.

I. INTRODUCTION

SYNTHETIC aperture radar (SAR) satellites continuously monitor the Earth from space and retrieve important information about dielectric and structural properties of the objects on the surface. In contrast to optical sensors that are affected by clouds, SAR is weather-independent and enables the acquisition of systematic and reliable time series. SAR systems

Received 30 September 2025; revised 11 March 2026; accepted 14 April 2026. Date of publication 22 April 2026; date of current version 4 May 2026. The work of Nikita Basargin was supported by the Helmholtz Association under the joint research school Munich School for Data Science (MUDS). (Corresponding author: Nikita Basargin.)

Nikita Basargin is with the Microwaves and Radar Institute, German Aerospace Center (DLR), 82234 Weßling, Germany, and also with the TUM School of Life Sciences, Technical University of Munich (TUM), 85354 Freising, Germany (e-mail: nikita.basargin@dlr.de).

Alberto Alonso-González is with the Signal Theory and Communications Department, Technical University of Catalonia (UPC), 08034 Barcelona, Spain (e-mail: alberto.alonso-gonzalez@upc.edu).

Irena Hajnsek is with the Microwaves and Radar Institute, German Aerospace Center (DLR), 82234 Weßling, Germany, and also with the Institute of Environmental Engineering, ETH Zürich, 8049 Zürich, Switzerland (e-mail: irena.hajnsek@dlr.de).

Digital Object Identifier 10.1109/TGRS.2026.3686699

can provide different data dimensions, including polarization, incidence angle variability, baselines between flight tracks, subapertures, frequency bands, and time series of acquisitions. Analyzing these datasets requires advanced algorithms and provides valuable information for different applications [1]. Classical techniques like polarimetry [2], interferometry [3], or tomography [4] focus on a single data dimension. In recent years, more advanced methods combining multiple data dimensions have been developed, for example, polarimetric interferometry [5] or the sum of Kronecker products (SKPs) decomposition [6].

Multidimensional SAR datasets are becoming increasingly available through experimental airborne campaigns and recently launched missions like BIOMASS [7], supporting the development of future SAR systems and calling for new methods to jointly analyze multiple dimensions. Tensor decompositions offer a direct way to process multidimensional data and are increasingly used across different research areas [8]. The remote sensing community actively uses tensor decompositions for hyperspectral data analysis [9]. In recent years, the concepts started to enter the SAR domain [10], [11], [12]. The classical tensor decompositions [13], [14], [15] are algebraic, i.e., they do not impose physical constraints on the solution. Recently, SAR-specific constrained variants have been proposed [16].

An advantage of the SAR domain is the availability of many physical models that explain the SAR signal properties for different data dimensions and applications. The physical models provide a link between the signal and the underlying geophysical parameters, for example, forest height [17], forest biomass [18], sea ice topography [19], and others. The current models explain some of the data dimensions, and it may be difficult to extend them to others directly. The integration with tensor decompositions is a promising direction since it enables the combination of different physical models for each dimension into a single framework. So far, this integration is largely unexplored.

In this article, we address this gap by combining concepts from algebraic model-free tensor decompositions with physical SAR models. From the perspective of SAR, this step generalizes matrix-based methods (e.g., polarimetric decompositions [2], [20], [21]) to tensor-based methods operating on a larger observation space and, therefore, capable of reducing ambiguities and inverting more complex models with additional parameters. From the perspective of model-free tensor decompositions, we impose additional

model-based constraints and require a physically interpretable solution.

We focus on high-resolution estimation of soil moisture, an important geophysical parameter for hydrology [22] and agriculture [23]. Soil moisture estimation is an active research area with a large number of proposed methods that can be categorized by the data dimensions. Some works focus on the backscatter intensity [24], [25], [26], [27], while others exploit time series of acquisitions for short-term change detection [28], [29], or differential interferometry [30], [31], [32]. While promising results have been obtained over bare areas, the estimation of soil moisture in the presence of vegetation still remains challenging. To improve the separation of the ground and vegetation signals, several works proposed to include polarimetry in combination with physical models [33], [34], [35]. Furthermore, polarimetric data have been used as an input to machine learning models [36], [37] or in methods combining physical modeling with machine learning [38], [39].

In this work, we include polarimetry as our main data dimension to enable soil moisture estimation under vegetation. Section II introduces the relevant concepts of SAR polarimetry, describes the datasets, and discusses polarimetric physical models that account for both the ground and the vegetation scattering. Since polarimetric data is typically stored as matrices, an extension to tensors is required to combine polarimetry with additional data dimensions. Section III covers multidimensional data, combines the physical models with tensor decompositions, and describes a general model inversion strategy based on numerical optimization. Section IV analyzes the model sensitivity and discusses single-matrix inversion ambiguities. We show that the temporal and spatial data dimensions have different information content and demonstrate that the expanded observation space reduces inversion ambiguities and allows the estimation of more physical parameters. In Section V-A, we focus on geophysical parameter estimation and formulate a soil moisture inversion algorithm from multitemporal polarimetric data. We validate the algorithm using airborne SAR data in the presence of changing vegetation and quantify the performance over different crop types. Furthermore, in Section V-B, we propose a method to estimate crop-specific polarimetric scattering signatures from the data and analyze the temporal behavior of polarimetric scattering mechanism power ratios. Section VI discusses the different data dimensions and physical models for other applications. Section VII concludes this article.

II. SAR POLARIMETRY

In this article, polarimetry is the main data dimension enabling the separation of ground and vegetation scattering. This section discusses the polarimetric data format and properties, introduces the datasets, and summarizes the relevant polarimetric physical models for soil moisture estimation.

Fully polarimetric SAR systems measure the complex-valued scattering coefficients of the four combinations of the transmitted and received, horizontal (H) and vertical (V) polarizations, and obtain the scattering matrix $\mathbf{S} \in \mathbb{C}^{2 \times 2}$ for every pixel

$$\mathbf{S} = \begin{bmatrix} S_{HH} & S_{HV} \\ S_{VH} & S_{VV} \end{bmatrix}. \quad (1)$$

\mathbf{S} is symmetric in monostatic configurations ($S_{HV} = S_{VH}$) [1]. Commonly, the coefficients are grouped into the scattering vector \mathbf{k} in the Pauli basis [40]

$$\mathbf{k} = \frac{1}{\sqrt{2}} \begin{bmatrix} S_{HH} + S_{VV} \\ S_{HH} - S_{VV} \\ S_{HV} + S_{VH} \end{bmatrix}. \quad (2)$$

Compared to the lexicographic basis, the Pauli basis carries the same information but offers a simpler physical interpretation. The matrix \mathbf{S} and the vector \mathbf{k} completely describe deterministic scatterers.

In the distributed scattering scenario, each resolution cell contains a large number of individual scatterers, and the vector \mathbf{k} follows a zero-mean complex Gaussian distribution [41]. Therefore, the scattering process has to be characterized statistically, using the coherency matrix $\mathbf{T} \in \mathbb{C}^{3 \times 3}$ in the Pauli basis to describe the second-order moment. \mathbf{T} is estimated from the data by combining n scattering vectors $\mathbf{k}^{(i)}$ from a close spatial neighborhood (typically the pixels within a local estimation window)

$$\mathbf{T} = \frac{1}{n} \sum_{i=1}^n \mathbf{k}^{(i)} \circ \mathbf{k}^{(i)*} \quad (3)$$

where \circ represents the outer product and $*$ denotes the complex conjugation. \mathbf{T} completely describes the polarimetry of distributed scatterers assuming the Gaussian distribution. By construction, \mathbf{T} is Hermitian, positive semi-definite (PSD), and has real and non-negative eigenvalues. We refer to the individual matrix elements with the index notation. For example, $\mathbf{T}_{[1,1]}$ denotes the matrix element found at index [1,1]. The diagonal elements $\mathbf{T}_{[m,m]}$ are real and nonnegative, while the off-diagonal elements are complex-valued.

A. F-SAR Datasets

The fully polarimetric L-band datasets used in this article were acquired with the airborne F-SAR [42] sensor by the German Aerospace Center (DLR) during two experimental campaigns.

The CROPEX 2014 campaign took place over the Wallerfing test site in southern Germany and provides seven L-band acquisitions covering a long-term period from May 15 to July 24. Ground teams accompanied the F-SAR flights to collect in situ soil moisture and vegetation measurements (e.g., biomass and crop height) over the selected fields. Surface soil moisture (top 5 cm) was measured at multiple positions across the fields using portable probes, with multiple samples taken at each position. Further details about the CROPEX 2014 campaign can be found in [43].

Fig. 1 shows a polarimetric time series over a maize field (outlined by the yellow boundary) with vegetation starting from a few centimeters and growing to about three meters in height. The change in the backscatter and polarimetric signature is strongly influenced by the vegetation growth, as illustrated by the Pauli RGB images (middle row). Early dates appear blue (HH + VV polarization, related to surface) and relatively dark (weak backscatter). As the crops grow, red (HH - VV polarization, related to dihedral) and green (HV + VH polarization, related to volume) colors become dominant, and the total backscatter increases. The bottom row

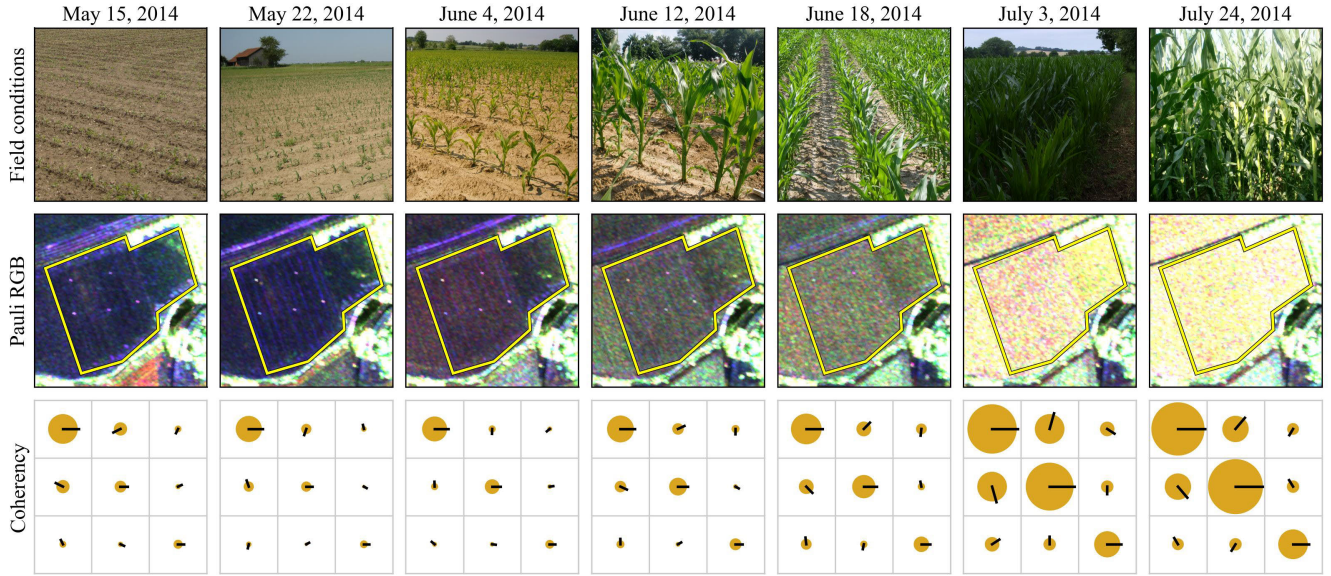


Fig. 1. Time series of polarimetric acquisitions over the maize field during the CROPEX 2014 campaign. (Top row) Photos of the crops taken during the in situ measurements. (Middle row) Pauli RGB images (HH + VV polarization in blue, HH - VV in red, and HV + VH in green) and field boundaries (in yellow). (Bottom row) Visualization of polarimetric coherency matrices averaged over the field. The circle area is proportional to the absolute element magnitude, and the line direction indicates the phase. For example, a real-valued positive number (phase 0°) points right, an imaginary number i (phase 90°) points up.

visualizes the elements of the 3×3 polarimetric coherency matrices estimated over the whole field, for each date. The element magnitude is proportional to the circle area, while the line direction indicates the phase. Larger circles illustrate the backscatter increase for the later dates. Despite the vegetation growth, as seen in Fig. 1, the reflection symmetry [44] assumptions commonly used for natural scatterers mostly hold with matrix elements $\mathbf{T}_{[1,3]}$ and $\mathbf{T}_{[2,3]}$ being small over time.

The second campaign, HTERRA 2022 (SARSimHT-NG), was performed in the province of Foggia in Italy, eight years later. Compared to CROPEX 2014, the data were acquired in a different climate zone, over fields with different irrigation practices, and at different incidence angles. The campaign provides a short-term time series with four flights in two days, acquired in April and then repeated in June. Several fields were irrigated before or during the campaign, leading to large soil moisture differences but similar vegetation between the acquisitions. Similar to the CROPEX campaign, in situ soil moisture and vegetation measurements have been collected for validation. More details about the HTERRA 2022 campaign can be found in [45].

B. Polarimetric and Dielectric Physical Models

Several physical models have been developed to connect physical parameters (e.g., soil moisture) to the SAR signal. This section provides an overview of the relevant polarimetric and dielectric models and the corresponding soil and vegetation parameters.

1) *Moisture to Dielectrics*: The radar signal is sensitive to the target's dielectrics, which are directly influenced by the moisture content. Several empirical models [46], [47] have been proposed to connect the volumetric (m^3/m^3) soil moisture w_s to the soil dielectrics ε_s . In this work, we use the model from [47] to convert the moisture w_s to the

complex-valued dielectrics ε_s

$$\text{HA}(w_s) = \varepsilon_s. \quad (4)$$

Internally, the model uses additional physical parameters including the radar frequency f and the soil texture (sand t_s and clay t_c contents), where the latter has a smaller influence compared to the moisture w_s . In this work, we constrain w_s to a feasible range from 5% to 45% and use the soil texture values from a reference database [48].

Considering the vegetation, the empirical relation proposed in [49] provides a mapping from the plant gravimetric (kg/kg) moisture content w_d to the complex-valued plant dielectrics ε_d

$$\text{UL}(w_d) = \varepsilon_d. \quad (5)$$

The empirical relation was established for maize leaves and is expected to be valid for several crop types. In this work, we constrain w_d to range between 50% and 70%.

2) *Polarimetric Surface Model*: The X-Bragg model [33], [50] describes the scattering from a slightly rough surface and has been used for bare soil. The model parameters are the soil dielectrics ε_s [derived from w_s using (4)], the radar incidence angle θ (known from geometry), the surface backscatter amplitude m_s , and a surface roughness depolarization term a_δ . In this work, we constrain a_δ to range between 15° and 75° .

The horizontal (H) and vertical (V) Bragg scattering coefficients B_H and B_V are given by

$$B_H = \frac{\cos \theta - \sqrt{\varepsilon_s - \sin^2 \theta}}{\cos \theta + \sqrt{\varepsilon_s - \sin^2 \theta}} \quad (6)$$

$$B_V = \frac{(\varepsilon_s - 1)(\sin^2 \theta - \varepsilon_s(1 + \sin^2 \theta))}{(\varepsilon_s \cos \theta + \sqrt{\varepsilon_s - \sin^2 \theta})^2}. \quad (7)$$

Then, the scattering intensity f_s and the ratio β are defined as

$$f_s = \frac{m_s^2}{2} |B_H + B_V|^2 \quad \beta = \frac{B_H - B_V}{B_H + B_V}. \quad (8)$$

Note that no additional non-negative constraints are required for m_s , since the term m_s^2 is always non-negative. Finally, the full X-Bragg coherency matrix \mathbf{T}_s is given by

$$\mathbf{T}_s = \mathbf{XB}(m_s, w_s, a_\delta) = f_s \begin{bmatrix} 1 & x_1^* & 0 \\ x_1 & x_2 & 0 \\ 0 & 0 & x_3 \end{bmatrix} \quad (9)$$

where

$$\begin{aligned} x_1 &= \beta \operatorname{sinc}(2a_\delta) & x_2 &= \frac{1}{2} |\beta|^2 (1 + \operatorname{sinc}(4a_\delta)) \\ \operatorname{sinc}(x) &= \frac{\sin x}{x} & x_3 &= \frac{1}{2} |\beta|^2 (1 - \operatorname{sinc}(4a_\delta)). \end{aligned} \quad (10)$$

3) *Polarimetric Dihedral Model*: The dihedral model describes a double reflection on two scattering planes and is adapted from [51]. In the context of soil moisture estimation, the two planes are the soil (s) and the vegetation stems, enabling the dihedral scattering (d). The model parameters are ε_s , θ , the dihedral scattering amplitude m_d , the vegetation dielectrics ε_d [derived from w_d using (5)], and the differential propagation phase a_φ introduced by the vegetation. Some previous works [33] fix the phase $a_\varphi = 0^\circ$, assuming no vegetation effects. In our case, we allow a_φ to influence the model and allow a range between -30° and 30° .

The local incidence angles for both scattering planes are given by

$$\theta_s = \theta \quad \theta_d = \frac{\pi}{2} - \theta. \quad (11)$$

The Fresnel coefficients for soil horizontal F_H^s , soil vertical F_V^s , stem (dihedral) horizontal F_H^d , and stem vertical F_V^d scattering are

$$F_H^{\{s,d\}} = \frac{\cos \theta_{\{s,d\}} - \sqrt{\varepsilon_{\{s,d\}} - \sin^2 \theta_{\{s,d\}}}}{\cos \theta_{\{s,d\}} + \sqrt{\varepsilon_{\{s,d\}} - \sin^2 \theta_{\{s,d\}}}} \quad (12)$$

$$F_V^{\{s,d\}} = \frac{\varepsilon_{\{s,d\}} \cos \theta_{\{s,d\}} - \sqrt{\varepsilon_{\{s,d\}} - \sin^2 \theta_{\{s,d\}}}}{\varepsilon_{\{s,d\}} \cos \theta_{\{s,d\}} + \sqrt{\varepsilon_{\{s,d\}} - \sin^2 \theta_{\{s,d\}}}}. \quad (13)$$

Then, the scattering intensity f_d and the ratio α are

$$f_d = \frac{m_d^2}{2} |F_H^s F_H^d + F_V^s F_V^d \exp(ia_\varphi)|^2 \quad (14)$$

$$\alpha = \frac{F_H^s F_H^d - F_V^s F_V^d \exp(ia_\varphi)}{F_H^s F_H^d + F_V^s F_V^d \exp(ia_\varphi)}. \quad (15)$$

Finally, the dihedral coherency matrix is given by

$$\mathbf{T}_d = \mathbf{DH}(m_d, w_s, w_d, a_\varphi) = f_d \begin{bmatrix} |\alpha|^2 & \alpha & 0 \\ \alpha^* & 1 & 0 \\ 0 & 0 & 0 \end{bmatrix}. \quad (16)$$

4) *Polarimetric Volume Model*: Volume scattering depends on several factors, including the vegetation type and phenological stage. Different volume models have been proposed (see [21], [33]), often approximating the vegetation as a cloud of particles with a specific shape and orientation. Some of the proposed volume coherency matrices include randomly oriented dipoles $\mathbf{T}_v^{\text{rnd}}$ or horizontally oriented dipoles $\mathbf{T}_v^{\text{hrz}}$

$$\mathbf{T}_v^{\text{rnd}} = \frac{1}{4} \begin{bmatrix} 2 & 0 & 0 \\ 0 & 1 & 0 \\ 0 & 0 & 1 \end{bmatrix} \quad \mathbf{T}_v^{\text{hrz}} = \frac{1}{30} \begin{bmatrix} 15 & -5 & 0 \\ -5 & 7 & 0 \\ 0 & 0 & 8 \end{bmatrix}. \quad (17)$$

More complex models employ a parametric form and require additional parameters [51].

In this work, we use randomly oriented dipoles $\mathbf{T}_v^{\text{rnd}}$ as the most general form of volume scattering applicable to a wide variety of crops. The matrix $\mathbf{T}_v^{\text{rnd}}$ scaled by the volume amplitude m_v in the volume model

$$\mathbf{T}_v = \mathbf{VL}(m_v) = \frac{m_v^2}{2} \mathbf{T}_v^{\text{rnd}}. \quad (18)$$

In addition, instead of using a predefined volume scattering matrix, we discuss the estimation of \mathbf{T}_v directly from the data with the proposed method in Section V-B.

C. Three-Component Model

Agricultural fields have a rather complex and dynamic polarimetric signature that depends on soil roughness, soil moisture, and the amount, type, and phenological stage of the vegetation. A single model-based component like X-Bragg is often not able to reconstruct the data well. Polarimetric model-based decompositions [52] typically use a sum of several components to approximate the coherency matrix \mathbf{T} . Similar to the approach in [33], we use a three-component model

$$\begin{aligned} \mathbf{T} &\approx \mathbf{XB}(m_s, w_s, a_\delta) \\ &\quad + \mathbf{DH}(m_d, w_s, w_d, a_\varphi) \\ &\quad + \mathbf{VL}(m_v). \end{aligned} \quad (19)$$

In the next step, we consider the number of observables and model parameters. All three model components are designed for natural scatterers and assume reflection symmetry [44]. The matrix elements $\mathbf{T}_{[1,3]}$ and $\mathbf{T}_{[2,3]}$ (and their conjugate counterparts $\mathbf{T}_{[3,1]}$ and $\mathbf{T}_{[3,2]}$) are assumed to be zero and ignored by the model. This leaves us with five observables: three real-valued elements on the diagonal and one complex-valued off-diagonal element $\mathbf{T}_{[1,3]}$. The observation space is further reduced when a purely real-valued model is used that is unable to fully represent the phase of $\mathbf{T}_{[1,2]}$.

In contrast, the three-component model in (19) has seven parameters: m_s , m_d , m_v , w_s , w_d , a_δ , and a_φ . Even more parameters are required if a parametric volume model is used. This can lead to an ambiguous inversion problem: there may exist different sets of parameters that result in the same or very similar reconstruction.

There are two major ways to deal with this ambiguity. The first option is to simplify the model and reduce the effective number of parameters. For example, components can be removed using specific criteria (e.g., by picking the dominant scattering mechanism), some parameters can be set to a reasonable fixed value, parameters can be constrained to a specific value range, or only certain combinations of parameter values can be allowed (e.g., orthogonal vectors). The second option is to expand the observation space by adding additional data dimensions while sharing some parameters along the new dimensions. This brings the advantage of being able to invert more parameters and, therefore, use more complex and accurate models. In this work, we combine both options to address the inversion ambiguities.

III. TENSORS

Tensors are multidimensional arrays that extend matrices to three or more dimensions and offer a natural way of

working with multidimensional data. In this article, we use the tensor formalism to combine polarimetry with additional data dimensions. Compared to an approach that reshapes data into matrices or vectors, using tensors provides a clear interpretation for each dimension and simplifies indexing. Furthermore, physical modeling is more flexible, as we can independently choose a different physical model for each data dimension. We follow the notation adapted from [8] with a few extensions. Bold lowercase letters, e.g., \mathbf{x} , represent 1-D vectors, bold capital letters, e.g., \mathbf{X} , indicate 2-D matrices, and calligraphic letters, e.g., \mathcal{X} , denote multidimensional tensors.

We refer to individual tensor elements with the index notation. Let $\mathcal{X} \in \mathbb{C}^{I_1 \times I_2 \times \dots \times I_N}$, then $\mathcal{X}_{[i_1, \dots, i_N]} \in \mathbb{C}$ denotes the individual elements of \mathcal{X} found at index $[i_1, \dots, i_N]$. A colon indicates all elements along a dimension, similar to rows or columns of a matrix. For example, let $\mathcal{Y} \in \mathbb{C}^{5 \times 3 \times 6}$, then $\mathcal{Y}_{[i, j, :]} \in \mathbb{C}^6$ is a vector found at index $[i, j]$, extending along the last dimension of \mathcal{Y} . Multiple colons indicate all elements along several dimensions, e.g., $\mathcal{Y}_{[:, :, i]} \in \mathbb{C}^{3 \times 6}$ denotes a matrix found at index $[i]$, extending along the second and the third dimensions of \mathcal{Y} .

The norm $\|\mathcal{X}\|$ of $\mathcal{X} \in \mathbb{C}^{I_1 \times I_2 \times \dots \times I_N}$ is given by

$$\|\mathcal{X}\| = \sqrt{\sum_{i_1=1}^{I_1} \sum_{i_2=1}^{I_2} \dots \sum_{i_N=1}^{I_N} |\mathcal{X}_{[i_1, i_2, \dots, i_N]}|^2} \quad (20)$$

and is equivalent to the Frobenius norm in the 2-D case.

A. Algebraic Tensor Decompositions

Algebraic tensor decompositions extend matrix factorization methods, e.g., the singular value decomposition (SVD) [53], and directly operate on multidimensional tensors. We consider the algebraic decompositions to be model-free, as they do not enforce a specific physical meaning or assign a model to each component. Two commonly used methods are the canonical polyadic (CP) [13], [14], and Tucker [15] decompositions. A detailed review of tensor decompositions can be found in [8].

This work extends the CP decomposition with model-based physical components. The original model-free formulation factorizes a d -dimensional tensor \mathcal{X} into a sum of R components. Each component is an outer product of d factor vectors. In the 3-D case ($d = 3$), the decomposition of $\mathcal{X} \in \mathbb{C}^{I \times J \times K}$ is defined as

$$\mathcal{X} \approx \sum_{r=1}^R \mathbf{a}_r \circ \mathbf{b}_r \circ \mathbf{c}_r \quad (21)$$

where $\mathbf{a}_r \in \mathbb{C}^I$, $\mathbf{b}_r \in \mathbb{C}^J$, and $\mathbf{c}_r \in \mathbb{C}^K$ are the factor vectors. The factors run along different dimensions and are an important concept for this work.

B. Model-Based Tensor Decompositions

In this article, we combine tensor decomposition concepts with the physical SAR models to define a model-based tensor decomposition. Several possible SAR data dimensions can be combined: polarimetry, interferometry, time series, incidence angle diversity, subapertures, multifrequency acquisitions, or spatial variability. The criteria for picking data dimensions mainly depend on data availability and the capabilities of the physical model to use the information along the new

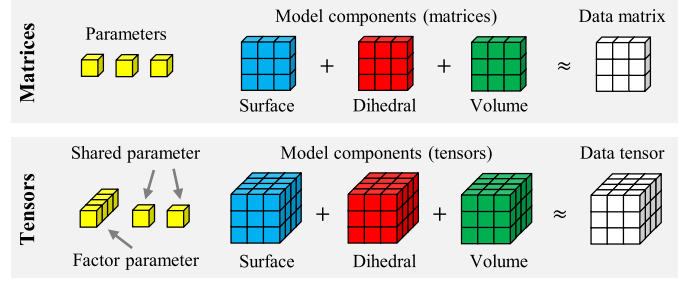


Fig. 2. Expansion from matrices (top) to tensors (bottom). Shared parameters are constant while factor parameters are allowed to have different values along the new data dimension.

dimension. In this article, we demonstrate the combination of polarimetry with temporal and spatial dimensions.

In general, we extend the observation space from a single polarimetric coherency matrix $\mathbf{T} \in \mathbb{C}^{3 \times 3}$ to a multidimensional tensor \mathcal{D} , for example, a stack of N matrices resulting in a data tensor $\mathcal{D} \in \mathbb{C}^{N \times 3 \times 3}$. Fig. 2 illustrates the decomposition expansion from matrices to tensors. The decomposition problem becomes

$$\mathcal{D} \approx \mathcal{R} = \mathcal{C}_s + \mathcal{C}_d + \mathcal{C}_v \quad (22)$$

where the data tensor \mathcal{D} is approximated by the model reconstruction \mathcal{R} . The three component tensors \mathcal{C}_s , \mathcal{C}_d , \mathcal{C}_v are internally using the surface, dihedral, and volume models from Section II-B, respectively.

Similar to expanding the data, we expand some of the parameters driving the physical models. We distinguish between *shared* parameters that have the same value and *factor* parameters that are allowed to have different values along the new data dimensions. Choosing which parameters are shared is an important step and requires setting assumptions. For example, when working with a time series with N acquisitions, we may assume that the soil roughness remains similar (shared parameter $a_\delta \in \mathbb{R}$) while the soil moisture changes for every acquisition (factor parameter $\mathbf{w}_s \in \mathbb{R}^N$). When more than one dimension is added, parameters can be chosen to be factors along some of the dimensions and remain shared along others. For example, soil moisture can vary over time but be shared across pixels within a small spatial neighborhood.

C. Inversion With Numerical Optimization

The physical models discussed in this article are forward models: functions that map the parameters to polarimetric coherency matrices or tensors approximating the data. The inverse problem considers the reverse direction of going from the data to the physical parameters, an important topic for practical applications. Many previous works present a specific model together with a specific way to invert it. In this article, we adopt a more general approach for model inversion based on optimization.

The main objective is to find a set of physical parameters that provides a good reconstruction of the data. A distance metric (also called the loss function) is required to evaluate the quality of the reconstruction. The distance metric is a function that takes two tensors (e.g., data and reconstruction) and returns a single real number indicating the distance between

them. In this article, we use the squared error loss function that can be expressed with the matrix norm in (20)

$$\|\mathcal{D} - \mathcal{R}\|^2. \quad (23)$$

This loss function is also minimized by the standard CP decomposition or by low-rank approximations based on the SVD, such as the SKP decomposition [6]. It should be noted that the choice of the loss function makes implicit assumptions on the data distribution [54]. For polarimetric data, several specialized distance metrics exist, and an overview is provided in [55]. In the context of model-based tensor decompositions, any differentiable loss function can be used, and we pick the squared error loss in (23) for its simplicity and low computational cost.

We treat the inversion as a constrained optimization problem and minimize the distance between the data tensor \mathcal{D} and the model reconstruction \mathcal{R} subject to model-dependent constraints (e.g., feasible parameter ranges)

$$\arg \min_{\text{parameters}} \|\mathcal{D} - \mathcal{R}\|^2. \quad (24)$$

There are several minimization methods available, and in this article, we use an iterative method based on gradient descent. Each iteration, we adjust the model parameters based on the gradient with respect to the loss function, taking into account the constraints. The minimization is implemented in PyTorch [56] and uses the first-order Adam optimizer [57]. The gradients are computed using automatic differentiation, and there is no need to provide analytical expressions for each parameter.

This inversion approach has several advantages. First, iterative optimization allows fine control over parameter constraints to ensure physical validity. The constraints may range from simple rules like minimum and maximum bounds (e.g., to ensure the inverted physical parameters stay within a reasonable range) to more advanced concepts like manifolds of PSD matrices [58]. Second, there is no need to define an explicit inversion algorithm as it is implicitly defined through the optimization of the loss function. This avoids the pitfall of prioritizing some model components over others, for example, by first inverting the volume model parameters that may result in a nonphysical residual surface component. Third, the inversion strategy remains the same for different physical models or applied constraints. This allows for focus on experimentation and model improvements without the need to adjust the inversion algorithm after each model or constraint change.

At the same time, numerical optimization based on gradient descent has some limitations. The optimizer can converge to a local minimum if the combination of the physical model and the loss function is not convex. Some physical models may provide a combination of very large and very small gradients for different model parameters, resulting in a complicated loss landscape and slowing down the convergence. Related to that is the relatively high computational cost proportional to the number of iterations. In this article, we use 500 iterations in most experiments.

The challenges can be addressed in several ways. Stricter constraints and regularization can help to eliminate the local minima and make the optimization problem convex. For nonconvex problems, it is possible to run the optimizer

several times with different starting conditions and hyperparameters (e.g., the learning rate) and then choose the best solution. Finally, adjusting the optimizer hyperparameters and using reasonable starting conditions can speed up the convergence. The tensor formalism simplifies implementation and is a natural choice for efficient parallelization on GPUs, partially offsetting the computational cost of optimization.

IV. MODEL SENSITIVITY AND AMBIGUITIES

The inversion of the three-component model from Section II-C is ambiguous when the model achieves the same minimal distance to the data with *different* sets of physical parameters. When inverting a single polarimetric matrix, the same reconstruction loss can be achieved with different moisture values by adjusting other parameters. In this section, we illustrate this issue by examining the loss landscapes and show that the extension of the observation space from matrices to tensors reduces the inversion ambiguities and improves the sensitivity to soil moisture.

A. Polarimetric-Spatial Ambiguity Reduction

In the first example, we combine polarimetry with spatial variability to increase the number of observables. The main benefit of the spatial dimension is that only a single SAR image is required. To form the data tensor, we define N adjacent nonoverlapping spatial patches, estimate a coherency matrix for each patch, and stack the matrices into the polarimetric spatial tensor $\mathcal{D}^{\text{PS}} \in \mathbb{C}^{N \times 3 \times 3}$. In this experiment, each spatial patch is 8×8 m in size, resulting in 80 independent looks per patch. The spatial grid is shown on the left of Fig. 3, where the central patch is marked in red. A different number of patches can be combined into the tensor \mathcal{D}^{PS} . In this section, we compare inversion ambiguities for a single patch ($N = 1$, equivalent to inverting a single matrix), $N = 25$ patches, and $N = 81$ patches.

Regarding the model parameters, we assume that soil conditions (moisture and roughness) do not vary significantly between adjacent patches in the field. At the same time, motivated by the high resolution of the F-SAR system, we allow differences in the vegetation and backscatter: some patches may have taller plants with stronger dihedral and volume backscatter. These assumptions lead to shared parameters w_s , w_d , a_δ , a_φ and factors \mathbf{m}_s , \mathbf{m}_d , $\mathbf{m}_v \in \mathbb{R}^N$. The model approximates the data \mathcal{D}^{PS} by the reconstruction \mathcal{R}^{PS} . Each reconstruction slice $\mathcal{R}_{[i,:]}^{\text{PS}}$ is given by

$$\begin{aligned} \mathcal{R}_{[i,:]}^{\text{PS}} = & \text{XB}(\mathbf{m}_{s[i]}, w_s, a_\delta) \\ & + \text{DH}(\mathbf{m}_{d[i]}, w_s, w_d, a_\varphi) \\ & + \text{VL}(\mathbf{m}_{v[i]}). \end{aligned} \quad (25)$$

To study the inversion ambiguities, we consider the landscape of the loss function (distance between the data and the reconstruction) for different values of the input physical parameters. Since the model has $3N + 4$ parameters in total, visualizing the whole loss landscape is not feasible. However, we can visualize a 2-D slice by fixing two of the parameters and finding the optimal values for the others. We set the shared moisture w_s and the surface amplitude for the central

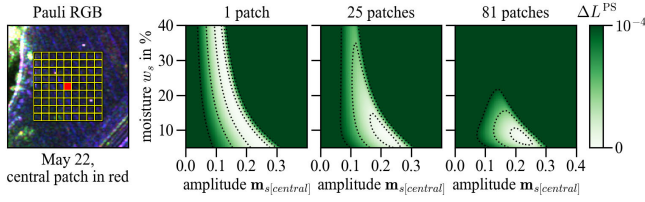


Fig. 3. Comparison of inversion ambiguities for a different number of jointly inverted matrices from adjacent spatial patches. Inverting a single matrix is ambiguous since the same optimal loss can be obtained with different moisture values. With more matrices, the ambiguities are reduced, and the white regions where the loss is close to the optimum become smaller. The left plot shows the placement of the spatial patches.

patch $\mathbf{m}_{s[central]}$ to fixed values x, y , and solve the following constrained optimization problem to obtain the loss L^{PS} :

$$L^{PS}(x, y) = \min_{\substack{\mathbf{m}_s, \mathbf{m}_d, \mathbf{m}_v, \\ w_s, w_d, a_\delta, a_\varphi}} \|\mathcal{D}^{PS} - \mathcal{R}^{PS}\|^2$$

$$\text{s.t. } \mathbf{m}_{s[central]} = x$$

$$w_s = y. \quad (26)$$

Then, we analyze the loss difference ΔL^{PS} between L^{PS} and the overall optimal loss (across all possible combinations of w_s and $\mathbf{m}_{s[central]}$)

$$\Delta L^{PS}(x, y) = L^{PS}(x, y) - \min_{x', y'} L^{PS}(x', y'). \quad (27)$$

Fig. 3 compares the resulting ΔL^{PS} landscapes for a different number of jointly inverted patches. White areas indicate combinations of fixed w_s and $\mathbf{m}_{s[central]}$ achieving the overall optimal loss. It becomes evident that the inversion of a single patch is ambiguous, since different values of w_s can be picked, resulting in the same optimal loss (white region in Fig. 3). In contrast, jointly inverting multiple patches reduces the size of the white area and indicates a more compact minimum.

Provided that there is variability across the spatial patches, using more patches imposes stricter constraints and is more effective in reducing the inversion ambiguities. The downside of this approach is the reduced spatial resolution of the estimated shared parameters. In terms of the spatial area, the resolution of shared parameters is reduced by the factor of N as only one parameter value is estimated across all N patches.

B. Polarimetric-Temporal Ambiguity Reduction

When a time series of SAR images is available, ambiguities can also be reduced using the temporal dimension to avoid the loss of spatial resolution. The polarimetric-temporal data tensor $\mathcal{D}^{PT} \in \mathbb{C}^{N \times 3 \times 3}$ is a stack of coherency matrices estimated from the same spatial patch but at N different times. The Pauli RGB time series used in this section is illustrated in Fig. 4.

The use of the temporal dimension requires setting different assumptions on what parameters can be shared. We allow soil moisture \mathbf{w}_s and the vegetation-related backscatter amplitudes \mathbf{m}_d and \mathbf{m}_v to change over time (factor parameters), while the remaining parameters $m_s, w_d, a_\delta,$ and a_φ are shared across the acquisitions. The reconstructed time series tensor is

$$\mathcal{R}_{[i:\dots]}^{PT} = \mathbf{X}\mathbf{B}(m_s, \mathbf{w}_{s[i]}, a_\delta)$$

$$+ \mathbf{D}\mathbf{H}(\mathbf{m}_{d[i]}, \mathbf{w}_{s[i]}, w_d, a_\varphi)$$

$$+ \mathbf{V}\mathbf{L}(\mathbf{m}_{v[i]}). \quad (28)$$

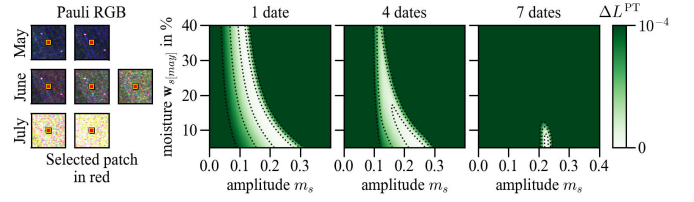


Fig. 4. Comparison of inversion ambiguities for a different number of jointly inverted matrices from different dates. With more dates, the ambiguities are reduced, and the white regions where the loss is close to the optimal become smaller. The left plot shows the field conditions around the same spatial patch at different dates.

For the ambiguity analysis, we fix the shared surface amplitude m_s and the soil moisture $\mathbf{w}_{s[may]}$ for one of the dates (May 22) to constant values x, y , and solve the following optimization problem to obtain the loss L^{PT} :

$$L^{PT}(x, y) = \min_{\substack{m_s, \mathbf{m}_d, \mathbf{m}_v, \\ w_s, w_d, a_\delta, a_\varphi}} \|\mathcal{D}^{PT} - \mathcal{R}^{PT}\|^2$$

$$\text{s.t. } m_s = x$$

$$\mathbf{w}_{s[may]} = y. \quad (29)$$

Then, we analyze the loss difference ΔL^{PT} between L^{PT} and the overall optimal loss (across all possible combinations of m_s and $\mathbf{w}_{s[may]}$)

$$\Delta L^{PT}(x, y) = L^{PT}(x, y) - \min_{x', y'} L^{PT}(x', y'). \quad (30)$$

We consider the model inversion to be *insensitive* to moisture when we can find moisture values that differ by more than 10% and still obtain a loss close to the optimum for both moisture values. Conversely, we consider the inversion to be *sensitive* to moisture, when changing the moisture value by 10% from the optimum significantly increases the reconstruction loss. For example, the inversion using a single date ($N = 1$, equivalent to inverting a single matrix) in Fig. 4 is ambiguous and insensitive to moisture as we can pick any moisture value from 5% to 40% and obtain a small ΔL^{PT} , staying in the white area. A short time series with the first four dates reduces the ambiguous area but does not provide enough variability. In contrast, the joint inversion of seven dates provides a compact minimum and is sensitive to moisture, as a change of moisture by 10% from the optimum increases the loss (large ΔL^{PT} , green area).

Comparing Figs. 3 and 4, we observe that the temporal dimension provides a better ambiguity reduction than the spatial dimension, due to higher variability in the time series compared to the adjacent spatial patches, as well as different assumptions on shared and factor parameters. Here, using seven patches from different dates is more effective than using 81 adjacent patches from the same date.

C. Polarimetric-Temporal Moisture Sensitivity

In this section, we expand the soil moisture sensitivity analysis from a single location to a larger agricultural area. The polarimetric-temporal model (Section IV-B) and a joint inversion of several dates are used to reduce ambiguities.

To quantify the sensitivity over a larger area, we perform the following experiment. First, we invert the model to obtain

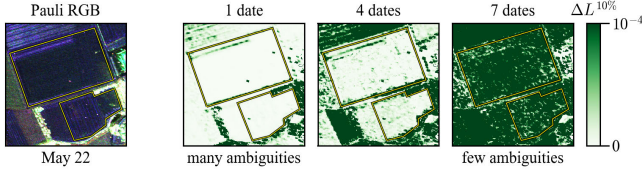


Fig. 5. Change in the loss value when the soil moisture for a single flight (May 22) is changed by 10% from the optimum. Ambiguous pixels appear in white: the changed soil moisture value does not affect the loss. Well-defined pixels appear in green: the loss increases when soil moisture is no longer optimal. Inverting a longer time series reduces the ambiguities and results in more well-defined green pixels.

the optimal soil moisture \mathbf{w}_s for each date and pixel. Then, we change the moisture $\mathbf{w}_{s[\text{may}]}$ for one selected date (May 22) by $\pm 10\%$ and rerun the optimization with $\mathbf{w}_{s[\text{may}]}$ fixed to that value. Rerunning the optimization allows the other parameters to adjust to the fixed moisture value and find a new loss minimum. Finally, we plot the loss difference $\Delta L^{10\%}$ between the optimal and changed moisture values for each pixel in Fig. 5. White indicates areas where the inversion is insensitive to moisture: change of soil moisture by 10% on the selected date does not affect the loss ($\Delta L^{10\%} \approx 0$). Green indicates pixels where the moisture is well-defined and cannot be arbitrarily changed without increasing the loss.

Results in Fig. 5 are consistent with Fig. 4. The inversion of a single matrix is ambiguous, while a longer time series with sufficient variability provides a well-defined inversion solution for most pixels.

V. GEOPHYSICAL PARAMETER RETRIEVAL

The previous section demonstrated the usefulness of a joint multidimensional data inversion. In this section, we move to more practical applications and demonstrate the inversion of geophysical parameters. First, we discuss soil moisture retrieval and irrigation detection. Then, we move to the polarimetric volume signature estimation. Finally, we discuss the component powers and the scattering ratios between different polarimetric mechanisms.

A. Soil Moisture Retrieval

In this section, we combine polarimetric, temporal, and spatial information to estimate soil moisture. We prepare the multidimensional input data as follows. First, we estimate the 3×3 polarimetric coherency matrices for each of the N dates and geocode the results onto the same spatial grid with $X \times Y$ pixels. In our experiments, we use a pixel spacing of 1 m, significantly oversampling the estimated coherency matrices (80 looks resulting in 8-m resolution). Then, we stack the data into a single polarimetric-spatial-temporal tensor $\mathcal{D}^{\text{PST}} \in \mathbb{C}^{X \times Y \times N \times 3 \times 3}$, where first two dimensions ($X \times Y$ pixels) represent the spatial information, the third dimension (N dates) runs over time, and the last dimensions represent the shape of each polarimetric coherency matrix (3×3).

1) *Polarimetric-Temporal-Spatial Model*: The assumptions on the parameters for the individual pixels are similar to the polarimetric-temporal model from Section IV-B. The surface scattering amplitude $\mathbf{M}_s \in \mathbb{R}^{X \times Y}$, the plant moisture $\mathbf{W}_d \in \mathbb{R}^{X \times Y}$, the surface depolarization $\mathbf{A}_\delta \in \mathbb{R}^{X \times Y}$, and the

differential phase $\mathbf{A}_\varphi \in \mathbb{R}^{X \times Y}$ are shared (constant) over time but vary in space across pixels. The remaining parameters vary both in space and time: the dihedral and volume scattering amplitudes $\mathcal{M}_d \in \mathbb{R}^{X \times Y \times N}$ and $\mathcal{M}_v \in \mathbb{R}^{X \times Y \times N}$, as well as the soil moisture $\mathcal{W}_s \in \mathbb{R}^{X \times Y \times N}$. The model reconstruction tensor is

$$\begin{aligned} \mathcal{R}_{[x,y,i,:]}^{\text{PST}} = & \text{XB} \left(\mathbf{M}_{s[x,y]}, \mathcal{W}_{s[x,y,i]}, \mathbf{A}_{\delta[x,y]} \right) \\ & + \text{DH} \left(\mathcal{M}_{d[x,y,i]}, \mathcal{W}_{s[x,y,i]}, \mathbf{W}_{d[x,y]}, \mathbf{A}_{\varphi[x,y]} \right) \\ & + \text{VL} \left(\mathcal{M}_{v[x,y,i]} \right). \end{aligned} \quad (31)$$

The spatial information is integrated through additional regularization of soil moisture, inspired by the total variation minimization [59]. We enforce a spatial smoothness constraint, preferring solutions where adjacent pixels (e.g., at indices $[x, y]$ and $[x + 1, y]$) have similar moisture values. Note that the regularization does not affect the temporal dimension, and soil moisture values between dates are not required to be similar. The regularization is not part of the model, but is enforced through a regularization term $r(\mathcal{W}_s)$

$$\begin{aligned} r(\mathcal{W}_s) = & \sum_{i=1}^N \sum_{x=1}^{X-1} \sum_{y=1}^{Y-1} \left(\mathcal{W}_{s[x,y,i]} - \mathcal{W}_{s[x+1,y,i]} \right)^2 \\ & + \left(\mathcal{W}_{s[x,y,i]} - \mathcal{W}_{s[x,y+1,i]} \right)^2 \end{aligned} \quad (32)$$

which is weighted by the regularization strength λ_w and added to the distance metric. Unless stated otherwise, we use $\lambda_w = 0.01$ in the experiments. Furthermore, we discuss the effect of the weight in Section V-A4. The resulting optimization problem is

$$\arg \min_{\substack{\mathbf{M}_s, \mathcal{M}_d, \mathcal{M}_v, \\ \mathcal{W}_s, \mathbf{W}_d, \mathbf{A}_\delta, \mathbf{A}_\varphi}} \left\| \mathcal{D}^{\text{PST}} - \mathcal{R}^{\text{PST}} \right\|^2 + \lambda_w \cdot r(\mathcal{W}_s). \quad (33)$$

2) *Validity Conditions*: After solving the optimization problem, the optimizer always provides a locally optimal solution, even when the model is not able to fit the data well. Therefore, it is important to define validity conditions and discard some solutions as invalid. There are several possibilities for defining such conditions. Since we focus on soil moisture retrieval, we regard all pixels as invalid where the inverted moisture reaches the minimal or maximal limit defined by the constraints. In our case, the feasible soil moisture range is between 5% and 45%. For those cases, the model is not able to explain the data well, and the moisture would further decrease or increase into an unfeasible region without the constraints.

3) *Soil Moisture Inversion Results*: Detailed soil moisture inversion results for the quinoa field of the HTERRA campaign are shown in Fig. 6. The time series combines four observations in April (bare surface) and four in June (quinoa and spontaneous vegetation). A part of the field indicated by the blue polygon was irrigated before the first acquisition in April and June, and is drying out during the following acquisitions. Each F-SAR acquisition was accompanied by in situ measurements used to validate the inverted soil moisture. The model successfully predicts high moisture in the irrigated area and low moisture in the dry area. Pixel-level predictions (8-m resolution) tend to have a high variability, and it is useful to average the samples over a region. Here, we average the

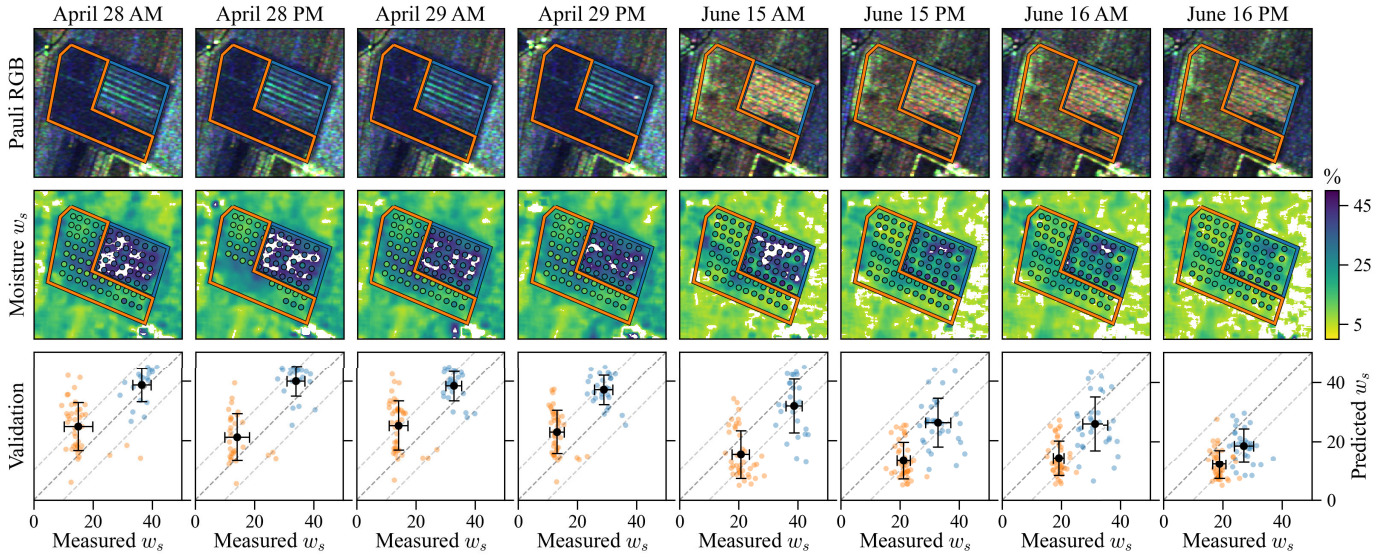


Fig. 6. Soil moisture inversion over the quinoa field during the HTERRA campaign. The top row shows the Pauli RGB images. The middle row shows the estimated soil moisture (invalid pixels discarded). The field is subdivided into the irrigated (blue polygon) and dry (orange polygon) areas. Small circles indicate positions of the in situ measurements and the measured soil moisture. The bottom row validates the in situ measurements against the estimated values. Blue and orange samples are from the irrigated and dry areas, respectively. Black points with error bars show the mean soil moisture and the standard deviation for all valid samples in the irrigated and dry areas. Coherency matrices are estimated with 80 looks and $\lambda_w = 0.01$.

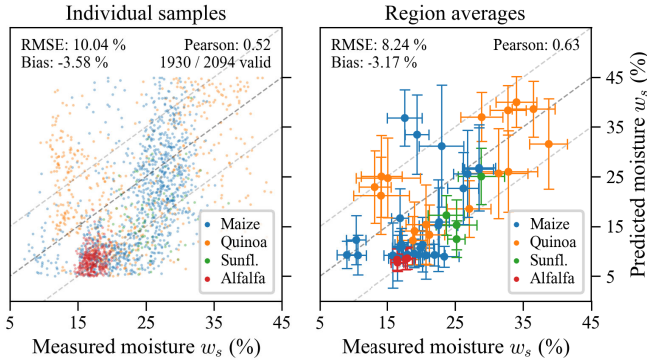


Fig. 7. Soil moisture inversion results for different fields and dates. The crop types include maize, alfalfa, sunflowers, and quinoa. The left plot shows individual (pixel-level) samples. The right plot shows region (field-level) statistics: all valid soil moisture samples are averaged to obtain the mean soil moisture and the standard deviation (indicated with error bars). Coherency matrices are estimated with 80 looks and $\lambda_w = 0.01$.

samples of the irrigated and dry areas to obtain field-level predictions (black points in the bottom row of Fig. 6).

A summary of soil moisture inversion results over fields with different crop types, including maize, alfalfa, sunflowers, and quinoa across the CROPEX and HTERRA campaigns, is shown in Fig. 7. The pixel-level predictions show a high variability and achieve an RMSE of 10%, while the field-level predictions obtained by averaging the samples over the field improve the RMSE to 8%. In both cases, the model tends to slightly underestimate the moisture with a bias of 3%–4%.

Note that the in situ measurements with portable sensors come with calibration and measurement uncertainties and may deviate from the moisture values in the field as seen by the radar. Furthermore, the radar signal penetrates into the ground to a certain depth that can be different compared to the depth sampled with the portable sensors.

In our experiments, we identified some crop types, including wheat, sugar beet, and cucumbers, where the model is not showing useful results, at least when it comes to the absolute soil moisture accuracy. For wheat, the model is sensitive to large moisture changes, allowing it to detect irrigation events as discussed in Section V-A5. For cucumbers and sugar beet, both test fields were located in near range (small incidence angle), where the polarimetric diversity might be insufficient to effectively separate the ground from vegetation.

4) *Effect of Multilook and Spatial Regularization:* The spatial resolution of the estimated moisture is directly affected by the size of the coherency matrix estimation window (multilook). Small windows are preferred for high-resolution products. However, if the number of samples (looks) in the window is small, the estimated coherency matrix does not accurately represent the signal statistics, leading to noisy moisture estimates. This effect is visible in the left column of Fig. 8 where a small number of looks leads to many invalid pixels with extreme moisture values. On the other hand, a larger number of looks creates a smoother map.

When spatial moisture regularization is added ($\lambda_w > 0$), the model is guided toward a solution with smoother moisture maps as well. This helps to close some of the invalid gaps and increases the inversion rate, which is defined as the percentage of samples that we consider valid. However, strong regularization might overly smooth the predictions, especially on the borders of irrigated regions.

To quantify the effect of multilooking and spatial regularization, we perform the inversion of all samples from Fig. 7 with different numbers of looks and λ_w , and report the metrics in Table I. Here, *sample* metrics refer to all pixels where we have the in situ measurements for validation, while *field* metrics refer to all samples averaged over the field or a region with similar conditions. For high-resolution pixel-level applications, it is preferred to have a high inversion rate and better sample

TABLE I
COMPARISON OF PERFORMANCE METRICS FOR A DIFFERENT NUMBER OF LOOKS AND REGULARIZATION STRENGTH

Setup		Sample metrics			Field metrics	
Looks	Regularization λ_w	Sample RMSE	Sample bias	Inversion rate (%)	Field RMSE	Field bias
20	0 (none)	10.65	-2.66	72.45	6.14	-2.56
20	0.01 (weak)	10.46	-5.48	91.02	8.24	-4.85
20	0.1 (strong)	10.17	-6.16	94.36	9.13	-5.37
80	0 (none)	10.35	-1.99	79.75	7.00	-2.27
80	0.01 (weak)	10.04	-3.58	92.17	8.24	-3.17
80	0.1 (strong)	9.98	-4.30	96.47	9.42	-3.63
320	0 (none)	10.13	-2.38	84.57	7.33	-2.32
320	0.01 (weak)	10.22	-2.42	92.26	9.15	-2.24
320	0.1 (strong)	9.94	-2.63	96.04	9.72	-2.47

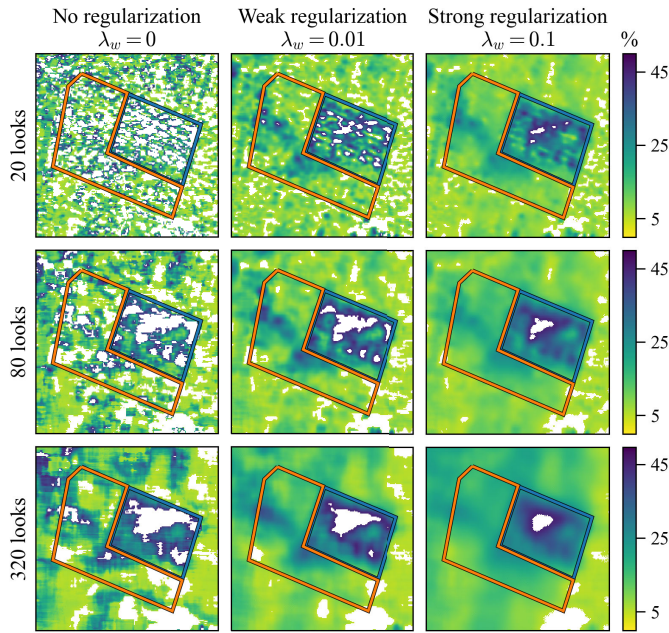


Fig. 8. Comparison of the estimated soil moisture values using different multilook and spatial regularization for the HTERRA quinoa field on June 15 (AM). Larger coherency matrix estimation window (multilook) and stronger spatial regularization (larger λ_w) lead to smoother soil moisture maps with fewer invalid pixels (gaps) but reduce the spatial details.

RMSE. This can be achieved by using a higher number of looks and strong regularization (larger λ_w). For field-level applications where only the average values over the whole field are important, it is useful to disable the spatial regularization. This lowers the inversion rate and creates more gaps. However, the remaining pixels provide more accurate moisture estimates with a better RMSE.

5) *Irrigation Detection*: In terms of the absolute soil moisture estimation accuracy, the proposed model does not provide accurate results for some growth stages of some crop types, including wheat. This can be the case when the signal from the vegetation and the ground cannot be separated or when the signal from the ground is too weak. However, great changes like irrigation can still be detected. To demonstrate this, we focus on an HTERRA wheat field that was irrigated before and during the first four flights in April. Fig. 9 shows the model

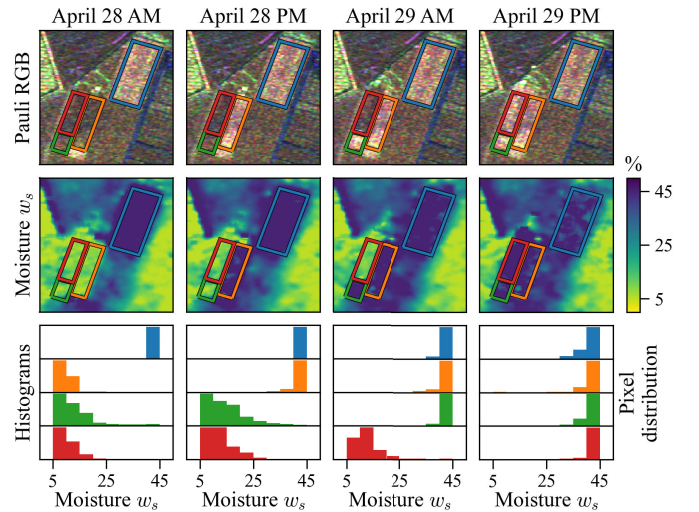


Fig. 9. Pauli RGB (top row), estimated soil moisture maps (middle row), and histograms (bottom row) over irrigated wheat fields during the HTERRA campaign. The blue polygon shows the area irrigated before the first flight. Orange, green, and red polygons indicate areas irrigated between the flights. The histograms show the predicted moisture distribution in the polygons with the matching color. The model is able to detect the irrigation events and predict high soil moisture after irrigation.

predictions for different areas indicated by colored polygons. The blue area was irrigated before the first flight and is slowly drying out. The orange area was irrigated between the first and the second flights, clearly showing a moisture increase between the two acquisitions. The green and the red areas correctly reflect irrigation between the following flights.

B. Polarimetric Volume Estimation

From the three model components, volume scattering from vegetation is the most challenging component, since it depends on many factors, including the crop type and the growth stage. In the previous experiments, we used a general form of volume scattering, randomly oriented dipoles \mathbf{T}_v^{nd} , to describe the volume scattering across all crop types. However, the vegetation can be modeled more accurately by using a crop-specific \mathbf{T}_v . In this section, we present a method to estimate \mathbf{T}_v from polarimetric time series combined with known soil and plant moisture values from the in situ measurements.

We form the field-wide polarimetric-temporal data tensor $\mathcal{D}^{\text{FPT}} \in \mathbb{C}^{N \times 3 \times 3}$ from coherency matrices averaged over a field at N different dates. The coherence matrices are estimated by combining all pixels from the whole field to get a good representation of the typical signal statistics. In this experiment, we use the time series over the CROPEX maize field as shown in Fig. 1.

The goal is to find a matrix $\mathbf{T}_v^{\text{maize}}$ that best reconstructs the observed data together with the model-based surface and dihedral components. We assume that the volume polarimetry remains similar over time, but its intensity may vary. Therefore, $\mathbf{T}_v^{\text{maize}}$ is a shared parameter constant over time, while the amplitude \mathbf{m}_v is a factor parameter allowed to have different values along the temporal dimension. An important consideration is the constraints imposed on $\mathbf{T}_v^{\text{maize}}$. The matrix must be Hermitian and PSD to ensure physical validity and interpretability. In addition, we restrict \mathbf{T}_v to be real-valued, similar to the volume models in Section II-B4. Finally, we require the matrix trace to be 1 to ensure that \mathbf{T}_v only describes the polarimetric scattering mechanism, while the scattering power is modeled by \mathbf{m}_v .

The constraints define a manifold of allowed matrices and can be enforced by a function that maps an unconstrained parameter set to the constrained manifold [58]. In this case, the unconstrained parameter is a 3×3 real matrix \mathbf{U} . The constraint function transforms \mathbf{U} to the constrained $\mathbf{T}_v^{\text{maize}}$ and is given by

$$\mathbf{T}_v^{\text{maize}} = \frac{\mathbf{U}\mathbf{U}^T}{\text{tr}(\mathbf{U}\mathbf{U}^T)}. \quad (34)$$

The product $\mathbf{U}\mathbf{U}^T$ is a 3×3 real PSD matrix by construction. Dividing the product by its trace (denoted by tr) results in the desired constrained mapping.

We account for the effect of soil and plant moisture on the signal by using the in situ measurements. Soil moisture varies over time and, therefore, is considered a factor parameter. We fix $\mathbf{w}_s \in \mathbb{R}^7$ to the in situ measurements averaged over the field. For the whole duration of the campaign, the plant moisture w_d was high (between 68% and 92%). Therefore, we use the highest available moisture value $w_d = 70\%$ supported by the model from [49]. Similar to the polarimetric-temporal model from Section IV-B, we assume the parameters m_s , a_δ , and a_φ shared over time, while the factor \mathbf{m}_d is allowed to vary. The reconstruction is given by

$$\begin{aligned} \mathcal{R}_{[i,:]}^{\text{FPT}} &= \text{XB}(m_s, \mathbf{w}_{s[i]}, a_\delta) \\ &+ \text{DH}(\mathbf{m}_{d[i]}, \mathbf{w}_{s[i]}, w_d, a_\varphi) \\ &+ \mathbf{m}_{v[i]} \cdot \frac{\mathbf{U}\mathbf{U}^T}{\text{tr}(\mathbf{U}\mathbf{U}^T)}. \end{aligned} \quad (35)$$

Using a free \mathbf{U} to describe the volume increases the number of parameters and can lead to inversion ambiguities when the time series does not offer enough variability. For the CROPEX maize time series, we apply regularization on a_φ , preferring a solution with a small differential propagation phase. In comparison, the previous work [33] ignores the phase difference under the assumption of a random volume layer and sets $a_\varphi = 0$. The regularization strength is set to a small number $\lambda_\varphi = 0.001$ and helps to avoid ambiguities between

the dihedral and the volume components. The resulting optimization problem is

$$\arg \min_{m_s, \mathbf{m}_d, \mathbf{m}_v, a_\delta, a_\varphi, \mathbf{U}} \|\mathcal{D}^{\text{FPT}} - \mathcal{R}^{\text{FPT}}\|^2 + \lambda_\varphi \cdot |a_\varphi|. \quad (36)$$

After solving the optimization problem, we obtain the unconstrained matrix \mathbf{U} and convert it to $\mathbf{T}_v^{\text{maize}}$ using (34), resulting in

$$\mathbf{T}_v^{\text{maize}} \approx \frac{1}{30} \begin{bmatrix} 20 & -7 & 0 \\ -7 & 2 & 0 \\ 0 & 0 & 8 \end{bmatrix}. \quad (37)$$

This solution is similar to the model-based horizontally oriented dipole model $\mathbf{T}_v^{\text{hrz}}$ from (17). By repeating this experiment for another maize field nearby, we obtain a similar result.

Provided in situ measurements and a polarimetric time series, the proposed model-based tensor decomposition framework can estimate \mathbf{T}_v for different crop types and incidence angles. This presents opportunities to improve the understanding of crop-specific volume scattering and suggest more accurate scattering models compared to randomly oriented dipoles.

C. Component Powers

The model-based decomposition represents the signal as a sum of three components and can be seen as a polarimetric decomposition similar to [21]. The main difference is the larger observation space, allowing the use of detailed component models with more parameters. Each component is associated with a specific scattering mechanism, allowing the characterization of the signal in terms of the power ratios. Given a coherency matrix \mathbf{T} , the signal power is given by its trace $\text{tr}(\mathbf{T})$. This concept can be extended to the tensor case.

First, we focus on average field statistics and consider polarimetric-temporal tensor $\mathcal{R}^{\text{FPT}} \in \mathbb{C}^{N \times 3 \times 3}$ from (35). The total power vector $\mathbf{p}^{\text{FPT}} \in \mathbb{R}^N$ is defined as

$$\mathbf{p}_{[i]}^{\text{FPT}} = \text{tr}(\mathcal{R}_{[i,:]}^{\text{FPT}}). \quad (38)$$

The power can also be computed for each individual model-based component. For example, the surface power $\mathbf{p}_s^{\text{FPT}}$ at a specific time i is given by

$$\mathbf{p}_{s[i]}^{\text{FPT}} = \text{tr}(\text{XB}(m_s, \mathbf{w}_{s[i]}, a_\delta)). \quad (39)$$

Fig. 10 illustrates the temporal dynamics of the surface, dihedral, and volume component powers obtained from the CROPEX maize field. In this decomposition, m_s is kept constant across time, and the only influence on the surface power comes from the soil moisture. During the CROPEX campaign, the volumetric soil moisture values averaged over the maize field ranged from 9% to 23%. We observe that the variation in the surface component power is rather small compared to the dihedral and volume power variations. Therefore, the estimation of soil moisture based only on the backscatter power is difficult, as the vegetation has a much stronger effect on the signal than the soil moisture. This illustrates the added value of polarimetric and temporal information.

The second observation is that the dihedral and volume powers grow significantly over time and are strongly correlated with the vegetation height during the growth phase of maize.

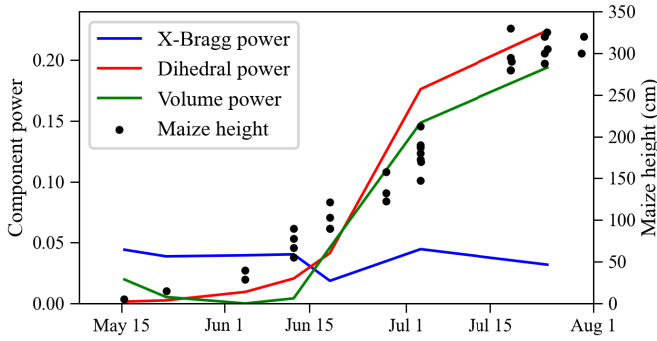


Fig. 10. Over the CROPEX maize field, the powers of the inverted dihedral (red) and volume (green) components show a correlation to the vegetation height (black points) measured during the ground campaign. The power of the X-Bragg component (blue) varies only with soil moisture.

This result indicates that the time series decomposition can, to a certain extent, separate the ground from the vegetation for the CROPEX maize time series. Therefore, we assume that $\mathbf{T}_v^{\text{maize}}$ obtained in (37) is representative for maize volume scattering over the field of study.

So far, this section has considered a time series of coherency matrices estimated over the whole field. For a more detailed spatial analysis, we use the polarimetric-spatial-temporal tensor $\mathcal{R}^{\text{PST}} \in \mathbb{C}^{X \times Y \times N \times 3 \times 3}$ (see (31) in Section V-A) that contains a different time series for every pixel. We compute the powers of each model-based component (surface, dihedral, and volume) for each pixel, normalize them by the total pixel power, and visualize them as a map. The normalized surface, dihedral, and volume power range between 0 and 1 and can be visualized in blue, red, and green, respectively. An example for the CROPEX maize time series is shown in Fig. 11. For the larger maize field, there are two different row orientations of the maize plants. Depending on the phenological stage of the plants, the row orientation can affect the dominant scattering mechanism across the field.

VI. DISCUSSION

A. Data Dimensions

SAR systems provide different data dimensions depending on the sensor and the acquisition setup. The type of information varies across the dimensions, with some data dimensions being more useful than others, depending on the application. In general, the framework presented in this article benefits most from data dimensions that offer the most variability, assuming the physical models can make use of that information. In this section, we discuss different data dimensions that can be integrated into the decomposition.

1) *Polarimetric*: PolSAR systems provide images in orthogonal transmit and receive polarizations with a larger information content compared to a single polarization. The main limitation is the availability of fully polarimetric (quad-pol) data. While many space-borne SAR systems have quad-pol capabilities, the operational mode typically only includes no or reduced (dual-pol) polarimetry because of the resolution or swath width tradeoffs. Recent SAR missions have shown positive developments. For example, ESA BIOMASS [7] provides quad-pol operational acquisitions.

We advocate for more operational quad-pol systems. First, polarimetric data provide sensitivity to different scattering

mechanisms and are important for ground-volume separation in the context of soil moisture estimation. Using only a single polarization is challenging, since the backscatter is significantly affected by the vegetation even for longer wavelengths (e.g., L-band). Second, several physical models (see Section II-B) have been developed for polarimetric data, providing a direct link between the SAR signal and geophysical parameters, and enabling explainable physics-based inversion. Third, polarimetric signatures can be estimated from data as shown in Section V-B, offering the potential to create better crop-specific models to improve soil moisture inversion, especially combined with recent advances in crop classification [60].

2) *Spatial*: Spatial information is naturally present in SAR images and can be exploited in several ways. A joint inversion of several adjacent patches improved the inversion stability in Section IV-A. In Section V-A, spatial regularization increased the inversion rate and provided smoother soil moisture maps. Spatial patterns can be explored furthermore, e.g., to perform segmentation [61], [62], [63] to avoid averaging the coherency matrices across field boundaries. In case of high-resolution systems, spatial information can be used to detect row structures that can significantly affect the backscatter signal [64], [65].

3) *Temporal*: A time series of acquisitions expands the observation space and enables addressing more problems than a single acquisition. Temporal information is often exploited for change detection [66], [67], and has been used for soil moisture estimation, usually focusing on short-term changes [28], [29], [68]. In contrast, the proposed method can make use of longer time series and separate the ground and vegetation contributions. To improve the separation, it is helpful to have a long time series that includes bare field conditions before the vegetation starts growing. Expanding the observation space with temporal information reduces the inversion ambiguities as demonstrated in Section IV-B.

Another research direction uses the temporal information for differential interferometry [30], [31], [32]. Here, the algorithms retrieve soil moisture by exploiting the phase between several zero-baseline acquisitions.

4) *Angular*: Several SAR techniques make use of the differences in the incidence or observation angles. Across-track interferometry [3] adds sensitivity to the vertical distribution of the scatterers. For datasets with several flight tracks, multibaseline interferometry and tomography [4] can further improve the ground-volume separation [43]. Larger differences in the incidence angles (e.g., ascending and descending orbits) also add variability that can be exploited for soil moisture estimation, often combined with other data dimensions including polarimetry [34] or time [69]. A further extension is circular SAR [70], [71], where the same target is observed from different angles and orientations, leading to an expanded observation space. While this imaging mode is not available with conventional satellites, SAR sensors mounted on UAV systems [72] offer a viable monitoring platform. Finally, the full bandwidth can be subdivided into several synthetic apertures to synthesize and jointly analyze multiple lower resolution images. A certain variability in the incidence angle, frequency, and time can be obtained with this approach,

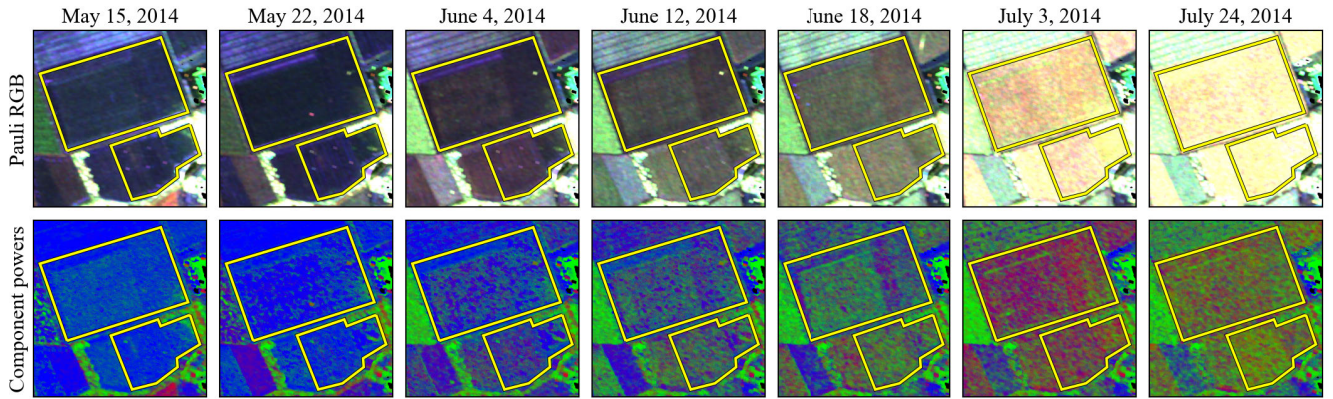


Fig. 11. Normalized component powers describe the ratios of the model-based scattering mechanisms (X-Bragg surface in blue, dihedral in red, and volume in green). Plant growth and phenological changes strongly affect the dominant scattering mechanism. Yellow polygons indicate the maize fields.

especially when using systems with a large bandwidth or a long integration time [73].

5) *Frequency*: Different frequency bands provide another data dimension. For example, L- and C-bands have different penetration depths into the medium and offer sensitivity to objects of different sizes. The approaches in [74] and [75] integrate information from several frequency bands and focus on backscatter amplitudes for moisture estimation. With operational and planned C- and L-band missions like ESA Sentinel-1, NASA-ISRO NISAR, and ESA ROSE-L, the frequency dimension is becoming more viable for operational use.

6) *Combining Dimensions*: A major benefit of the proposed model-based tensor decomposition framework is the ability to combine any number of data dimensions. While this requires making assumptions about shared and factor parameters, the inversion strategy remains the same: minimize the distance between the model reconstruction and the data. Techniques combining polarimetry with interferometry [5] or tomography [6] have been extensively explored in recent years and show an improved separation of the ground and volume signal contributions. Here, we see a potential for adding the temporal dimension to monitor changes over time in more detail. In addition, some interesting directions for future research include a joint analysis of polarimetric time series in multiple frequencies, or extension of multiangular multitemporal soil moisture estimation [69] with polarimetric models discussed in this article.

B. Geophysical Parameter Estimation in Different Domains

While this article focuses on soil moisture, the methodology can be extended to different applications where physical models for other parameters have been developed. In the context of forest height estimation, interferometric [17], [76], and polarimetric-interferometric models [5] are available, with extensions to biomass estimation in [18]. In the agricultural setting, models for crop height estimation based on interferometry are discussed in [77]. An approach for rice height estimation combining polarimetric, interferometric, and temporal information is discussed in [78]. Moving to the cryosphere, snow water equivalent estimation using differential interferometry and polarimetry is presented in [79]. Another approach for snow water equivalent estimation uses differential interferometry and squint angle diversity [80]. A model for

sea ice topography using polarimetric-interferometric data is discussed in [19].

Tensor formulation streamlines physical modeling by requiring independent models for each data dimension rather than a single complex model. This simplifies adaptation to a different domain, as only some model components need adjustment. Furthermore, adding a new data dimension only requires adding a model for that dimension.

C. Feature Extraction

Polarimetric data offers a rich information space with several model-free [20] and model-based [21], [81] polarimetric decompositions available. The proposed method can be seen as a novel model-based decomposition that operates on the expanded tensor observation space and uses more complex physical models compared to [21] to characterize the targets.

We see a potential to use the proposed model-based tensor decomposition as a feature extractor. As discussed in Section IV, the estimated features are less prone to inversion ambiguities (compared to features extracted from a single matrix) and are expected to be more robust. Furthermore, the extracted features compactly describe the input data; thus, the decomposition can be seen as a dimensionality reduction method.

The extracted parameters physically characterize the targets and can be provided as features to existing methods for image classification [82], [83], semantic segmentation [84], [85], superpixel segmentation [86], or target recognition [87], [88]. Depending on the domain (e.g., cryosphere, forests, and ocean), it is useful to integrate appropriate physical models into the decomposition to provide more meaningful features.

Considering change detection applications [66], [67], the proposed method accounts for the temporal dimension and provides temporal factors (or derived properties, such as component powers in Section V-C) that directly capture changes in specific parameters over time. In addition, the decomposition separates the signal from the ground and vegetation, allowing for the detection of specific changes (e.g., on the ground, ignoring the vegetation). Here, existing change detection techniques can be applied to the model-based components, similar to the approach in [16].

VII. CONCLUSION

Motivated by the increasing availability of multidimensional SAR data over the recent years, this work combines tensor

decompositions and physical models into a novel framework for geophysical parameter estimation. The proposed method takes advantage of the expanded observation space and jointly uses information from several data dimensions. For each data dimension and model parameter, the method allows setting different assumptions and defining whether the parameter is constant or can have different values along the dimension. With more observables, more model parameters can be inverted, enabling the use of more detailed models to cover a larger range of scenarios. This is especially important in agricultural areas, where different crop types and phenological stages strongly influence the scattering. Here, we approximate the signal by a sum of model components for the ground, the vegetation, and the dihedral interactions between them.

This work demonstrates a combination of polarimetry with the spatial and/or temporal dimensions, focusing on high-resolution soil moisture estimation under vegetation. Model inversion is formulated as a constrained optimization problem and relies on gradient-based numerical minimization. While computationally expensive, this inversion strategy brings flexibility with respect to the choice of constraints and data dimensions. The gradients are computed with automatic differentiation, allowing quick experimentation, e.g., setting new constraints or exchanging model components with any differentiable function.

Experimental results from two high-resolution airborne F-SAR campaigns demonstrate three main results. First, the joint inversion of several data dimensions effectively reduces inversion ambiguities. Considering individual data dimensions, the temporal dimension offers more variability and is more effective for ambiguity reduction compared to the spatial dimension. Second, the polarimetric, spatial, and temporal dimensions can be combined to retrieve soil moisture under several crop types, including maize, quinoa, alfalfa, and sunflowers. For some other crop types, including wheat, the model only shows sensitivity to great changes in moisture, allowing for the detection of irrigation. Third, the proposed method allows for the estimation of crop-specific volume scattering signatures when in situ soil moisture measurements are available. The method effectively separates the ground and volume scattering and shows a correlation of maize height with the volume and dihedral component powers.

Overall, model-based tensor decompositions open new ways to analyze multidimensional data, allow for extending existing methods with new data dimensions, and can be used in different application domains where physical SAR models are available. The proposed approach has the potential to enable improved geophysical parameter retrieval algorithms and suggest adjustments to the existing models to better fit the observed data.

ACKNOWLEDGMENT

The authors would like to thank the anonymous reviewers for giving valuable suggestions. Special thanks to Prof. Dr. Senthold Asseng for academic advice and discussions.

REFERENCES

- [1] A. Moreira, P. Prats-Iraola, M. Younis, G. Krieger, I. Hajnsek, and K. P. Papathanassiou, "A tutorial on synthetic aperture radar," *IEEE Geosci. Remote Sens. Mag.*, vol. 1, no. 1, pp. 6–43, Mar. 2013.
- [2] I. Hajnsek and Y.-L. Desnos, *Polarimetric Synthetic Aperture Radar: Principles and Application*, vol. 25. Cham, Switzerland: Springer, 2021.
- [3] R. Bamler and P. Hartl, "Synthetic aperture radar interferometry," *Inverse problems*, vol. 14, no. 4, p. R1, 1998.
- [4] A. Reigber and A. Moreira, "First demonstration of airborne SAR tomography using multibaseline L-band data," *IEEE Trans. Geosci. Remote Sens.*, vol. 38, no. 5, pp. 2142–2152, Sep. 2000. [Online]. Available: <https://ieeexplore.ieee.org/abstract/document/868873>
- [5] S. R. Cloude and K. P. Papathanassiou, "Polarimetric SAR interferometry," *IEEE Trans. Geosci. Remote Sens.*, vol. 36, no. 5, pp. 1551–1565, Sep. 1998. [Online]. Available: <https://ieeexplore.ieee.org/document/718859>
- [6] S. Tebaldini, "Algebraic synthesis of forest scenarios from multibaseline PolInSAR data," *IEEE Trans. Geosci. Remote Sens.*, vol. 47, no. 12, pp. 4132–4142, Dec. 2009.
- [7] S. Quegan et al., "The European space agency BIOMASS mission: Measuring forest above-ground biomass from space," *Remote Sens. Environ.*, vol. 227, pp. 44–60, Jun. 2019.
- [8] T. G. Kolda and B. W. Bader, "Tensor decompositions and applications," *SIAM Review*, vol. 51, no. 3, pp. 455–500, 2009.
- [9] M. Wang et al., "Tensor decompositions for hyperspectral data processing in remote sensing: A comprehensive review," *IEEE Geosci. Remote Sens. Mag.*, vol. 11, no. 1, pp. 26–72, Mar. 2023.
- [10] J. Kang, Y. Wang, and X. X. Zhu, "Multipass SAR interferometry based on total variation regularized robust low rank tensor decomposition," *IEEE Trans. Geosci. Remote Sens.*, vol. 58, no. 8, pp. 5354–5366, Aug. 2020.
- [11] J. Luo et al., "Despeckling multitemporal polarimetric SAR data based on tensor decomposition," *IEEE J. Sel. Topics Appl. Earth Observ. Remote Sens.*, vol. 16, pp. 9858–9873, 2023.
- [12] M. Leibovich, G. Papanicolaou, and C. Tsogka, "Synthetic aperture imaging and motion estimation using tensor methods," *SIAM J. Imag. Sci.*, vol. 13, no. 4, pp. 2213–2249, Jan. 2020.
- [13] J. D. Carroll and J.-J. Chang, "Analysis of individual differences in multidimensional scaling via an N-way generalization of 'Eckart-Young' decomposition," *Psychometrika*, vol. 35, no. 3, pp. 283–319, Sep. 1970.
- [14] R. A. Harshman et al., "Foundations of the PARAFAC procedure: Models and conditions for an 'explanatory' multimodal factor analysis," in *Proc. UCLA Work. Papers Phonetics*, 1970, p. 84.
- [15] L. R. Tucker, "Some mathematical notes on three-mode factor analysis," *Psychometrika*, vol. 31, no. 3, pp. 279–311, Sep. 1966.
- [16] N. Basargin, A. Alonso-González, and I. Hajnsek, "Constrained tensor decompositions for SAR data: Agricultural polarimetric time series analysis," *IEEE Trans. Geosci. Remote Sens.*, vol. 61, 2023, Art. no. 4410913. [Online]. Available: <https://ieeexplore.ieee.org/document/10313300>
- [17] F. Kugler, D. Schulze, I. Hajnsek, H. Pretzsch, and K. P. Papathanassiou, "TanDEM-X pol-InSAR performance for forest height estimation," *IEEE Trans. Geosci. Remote Sens.*, vol. 52, no. 10, pp. 6404–6422, Oct. 2014.
- [18] C. Choi, M. Pardini, J. Armston, and K. P. Papathanassiou, "Forest biomass mapping using continuous InSAR and discrete waveform LiDAR measurements: A TanDEM-X/GEDI test study," *IEEE J. Sel. Topics Appl. Earth Observ. Remote Sens.*, vol. 16, pp. 7675–7689, 2023.
- [19] L. Huang, G. Fischer, and I. Hajnsek, "Antarctic snow-covered sea ice topography derivation from TanDEM-X using polarimetric SAR interferometry," *Cryosphere*, vol. 15, no. 12, pp. 5323–5344, Dec. 2021.
- [20] S. R. Cloude and E. Pottier, "An entropy based classification scheme for land applications of polarimetric SAR," *IEEE Trans. Geosci. Remote Sens.*, vol. 35, no. 1, pp. 68–78, Jan. 1997. [Online]. Available: <https://ieeexplore.ieee.org/document/551935>
- [21] A. Freeman and S. L. Durden, "A three-component scattering model for polarimetric SAR data," *IEEE Trans. Geosci. Remote Sens.*, vol. 36, no. 3, pp. 963–973, May 1998.
- [22] H. Vereecken et al., "Soil hydrology in the Earth system," *Nature Rev. Earth Environ.*, vol. 3, no. 9, pp. 573–587, 2022.
- [23] X. Zhang, G. Feng, and X. Sun, "Advanced technologies of soil moisture monitoring in precision agriculture: A review," *J. Agricult. Food Res.*, vol. 18, Dec. 2024, Art. no. 101473.
- [24] P. C. Dubois, J. van Zyl, and T. Engman, "Measuring soil moisture with imaging radars," *IEEE Trans. Geosci. Remote Sens.*, vol. 33, no. 4, pp. 915–926, Jul. 1995.
- [25] W. Wagner, G. Lemoine, and H. Rott, "A method for estimating soil moisture from ERS scatterometer and soil data," *Remote Sens. Environ.*, vol. 70, no. 2, pp. 191–207, Nov. 1999.
- [26] K. Morrison and W. Wagner, "Explaining anomalies in SAR and scatterometer soil moisture retrievals from dry soils with subsurface scattering," *IEEE Trans. Geosci. Remote Sens.*, vol. 58, no. 3, pp. 2190–2197, Mar. 2020.

- [27] H. R. Mirsoleimani, M. R. Sahebi, N. Baghdadi, and M. El Hajj, "Bare soil surface moisture retrieval from Sentinel-1 SAR data based on the calibrated IEM and Dubois models using neural networks," *Sensors*, vol. 19, no. 14, p. 3209, Jul. 2019.
- [28] A. Balenzano, F. Mattia, G. Satalino, and M. W. J. Davidson, "Dense temporal series of C- and L-band SAR data for soil moisture retrieval over agricultural crops," *IEEE J. Sel. Topics Appl. Earth Observ. Remote Sens.*, vol. 4, no. 2, pp. 439–450, Jun. 2011.
- [29] A. Balenzano et al., "Sentinel-1 soil moisture at 1 km resolution: A validation study," *Remote Sens. Environ.*, vol. 263, Sep. 2021, Art. no. 112554.
- [30] F. De Zan, A. Parizzi, P. Prats-Iraola, and P. López-Dekker, "A SAR interferometric model for soil moisture," *IEEE Trans. Geosci. Remote Sens.*, vol. 52, no. 1, pp. 418–425, Jan. 2014.
- [31] S. Zwieback, S. Hensley, and I. Hajnsek, "Soil moisture estimation using differential radar interferometry: Toward separating soil moisture and displacements," *IEEE Trans. Geosci. Remote Sens.*, vol. 55, no. 9, pp. 5069–5083, Sep. 2017.
- [32] E. Wig, R. Michaelides, and H. Zebker, "Fine-resolution measurement of soil moisture from cumulative InSAR closure phase," *IEEE Trans. Geosci. Remote Sens.*, vol. 62, 2024, Art. no. 5212315. [Online]. Available: <https://ieeexplore.ieee.org/document/10526272>
- [33] I. Hajnsek, T. Jagdhuber, H. Schon, and K. P. Papathanassiou, "Potential of estimating soil moisture under vegetation cover by means of PolSAR," *IEEE Trans. Geosci. Remote Sens.*, vol. 47, no. 2, pp. 442–454, Feb. 2009.
- [34] T. Jagdhuber, I. Hajnsek, A. Bronstert, and K. P. Papathanassiou, "Soil moisture estimation under low vegetation cover using a multi-angular polarimetric decomposition," *IEEE Trans. Geosci. Remote Sens.*, vol. 51, no. 4, pp. 2201–2215, Apr. 2013.
- [35] A. Fluhrer et al., "Remote sensing of complex permittivity and penetration depth of soils using P-band SAR polarimetry," *Remote Sens.*, vol. 14, no. 12, p. 2755, Jun. 2022.
- [36] E. Santi, M. Daboor, S. Pettinato, and S. Paloscia, "Combining machine learning and compact polarimetry for estimating soil moisture from C-band SAR data," *Remote Sens.*, vol. 11, no. 20, p. 2451, Oct. 2019.
- [37] C. Lv et al., "Soil moisture retrieval over agricultural fields with machine learning: A comparison of quad-, compact-, and dual-polarimetric time-series SAR data," *J. Hydrol.*, vol. 644, Nov. 2024, Art. no. 132093.
- [38] R. Hänsch, T. Jagdhuber, and B. Fersch, "Soil-permittivity estimation under grassland using machine-learning and polarimetric decomposition techniques," *IEEE Trans. Geosci. Remote Sens.*, vol. 59, no. 4, pp. 2877–2887, Apr. 2021.
- [39] N. Basargin, A. Alberto Alonso-González, and I. Hajnsek, "Explainable physical PolSAR autoencoders for soil moisture estimation," in *Proc. IEEE/CVF Conf. Comput. Vis. Pattern Recognit. Workshops (CVPRW)*, Jun. 2025, pp. 2286–2295.
- [40] S. R. Cloude and E. Pottier, "A review of target decomposition theorems in radar polarimetry," *IEEE Trans. Geosci. Remote Sens.*, vol. 34, no. 2, pp. 498–518, Mar. 1996.
- [41] J. W. Goodman, "Some fundamental properties of speckle," *J. Opt. Soc. Amer.*, vol. 66, no. 11, pp. 1145–1150, 1976.
- [42] R. Horn, A. Nottensteiner, A. Reigber, J. Fischer, and R. Scheiber, "F-SAR—DLR's new multifrequency polarimetric airborne SAR," in *Proc. IEEE Int. Geosci. Remote Sens. Symp.*, Jul. 2009, pp. II-902–II-905. [Online]. Available: <https://ieeexplore.ieee.org/document/5418244>
- [43] H. Joerg, M. Pardini, I. Hajnsek, and K. P. Papathanassiou, "3-D scattering characterization of agricultural crops at C-band using SAR tomography," *IEEE Trans. Geosci. Remote Sens.*, vol. 56, no. 7, pp. 3976–3989, Jul. 2018.
- [44] S. Cloude, *Polarisation: Applications in Remote Sensing*. London, U.K.: Oxford Univ. Press, 2010.
- [45] A. Balenzano et al., "SARSimHT-NG campaign over southern Italy for investigating sub-daily water processes," in *Proc. IEEE Int. Geosci. Remote Sens. Symp. (IGARSS)*, Jul. 2024, pp. 4376–4379.
- [46] G. C. Topp, J. L. Davis, and A. P. Annan, "Electromagnetic determination of soil water content: Measurements in coaxial transmission lines," *Water Resour. Res.*, vol. 16, no. 3, pp. 574–582, Jun. 1980.
- [47] M. Hallikainen, F. Ulaby, M. Dobson, M. El-Rayes, and L.-K. Wu, "Microwave dielectric behavior of wet soil—Part I: Empirical models and experimental observations," *IEEE Trans. Geosci. Remote Sens.*, vol. GE-23, no. 1, pp. 25–34, Jan. 1985.
- [48] L. Poggio et al., "SoilGrids 2.0: Producing soil information for the globe with quantified spatial uncertainty," *SOIL*, vol. 7, no. 1, pp. 217–240, Jun. 2021.
- [49] F. T. Ulaby and M. A. El-Rayes, "Microwave dielectric spectrum of vegetation—Part II: Dual-dispersion model," *IEEE Trans. Geosci. Remote Sens.*, vol. GE-25, no. 5, pp. 550–557, Sep. 1987.
- [50] I. Hajnsek, E. Pottier, and S. R. Cloude, "Inversion of surface parameters from polarimetric SAR," *IEEE Trans. Geosci. Remote Sens.*, vol. 41, no. 4, pp. 727–744, Jun. 2003.
- [51] T. Jagdhuber, I. Hajnsek, and K. P. Papathanassiou, "An iterative generalized hybrid decomposition for soil moisture retrieval under vegetation cover using fully polarimetric SAR," *IEEE J. Sel. Topics Appl. Earth Observ. Remote Sens.*, vol. 8, no. 8, pp. 3911–3922, Aug. 2015.
- [52] S.-W. Chen, Y.-Z. Li, X.-S. Wang, S.-P. Xiao, and M. Sato, "Modeling and interpretation of scattering mechanisms in polarimetric synthetic aperture radar: Advances and perspectives," *IEEE Signal Process. Mag.*, vol. 31, no. 4, pp. 79–89, Jul. 2014.
- [53] C. D. Martin and M. A. Porter, "The extraordinary SVD," *Amer. Math. Monthly*, vol. 119, no. 10, pp. 838–851, 2012.
- [54] D. Hong, T. G. Kolda, and J. A. Duersch, "Generalized canonical polyadic tensor decomposition," *SIAM Rev.*, vol. 62, no. 1, pp. 133–163, Jan. 2020.
- [55] X. Qin et al., "Distance measures of polarimetric SAR image data: A survey," *Remote Sens.*, vol. 14, no. 22, p. 5873, Nov. 2022.
- [56] A. Paszke et al., "Automatic differentiation in PyTorch," Tech. Rep., 2017. [Online]. Available: <http://OpenReview.nethttps://openreview.net/forum?id=BJJsrmlfCZhttps://openreview.net/pdf?id=BJJsrmlfCZ>
- [57] D. P. Kingma and J. Ba, "Adam: A method for stochastic optimization," 2014, *arXiv:1412.6980*.
- [58] M. Lezcano Casado, "Trivializations for gradient-based optimization on manifolds," in *Proc. Adv. Neural Inf. Process. Syst.*, vol. 32, 2019, pp. 1–12. [Online]. Available: https://proceedings.neurips.cc/paper_files/paper/2019/file/1b33d16fc562464579b7199ca3114982-Paper.pdf
- [59] L. I. Rudin, S. Osher, and E. Fatemi, "Nonlinear total variation based noise removal algorithms," *Phys. D, Nonlinear Phenomena*, vol. 60, nos. 1–4, pp. 259–268, Nov. 1992.
- [60] A. Orynbaikyzy, U. Gessner, and C. Conrad, "Crop type classification using a combination of optical and radar remote sensing data: A review," *Int. J. Remote Sens.*, vol. 40, no. 17, pp. 6553–6595, Sep. 2019.
- [61] A. Alonso-Gonzalez, C. Lopez-Martinez, and P. Salembier, "Filtering and segmentation of polarimetric SAR data based on binary partition trees," *IEEE Trans. Geosci. Remote Sens.*, vol. 50, no. 2, pp. 593–605, Feb. 2012.
- [62] F. Qin, J. Guo, and F. Lang, "Superpixel segmentation for polarimetric SAR imagery using local iterative clustering," *IEEE Geosci. Remote Sens. Lett.*, vol. 12, no. 1, pp. 13–17, Jan. 2015.
- [63] W. Zhang, D. Xiang, and Y. Su, "Fast multiscale superpixel segmentation for SAR imagery," *IEEE Geosci. Remote Sens. Lett.*, vol. 19, pp. 1–5, 2022.
- [64] A. Beaudoin, T. Le Toan, and Q. H. J. Gwyn, "SAR observations and modeling of the C-band backscatter variability due to multiscale geometry and soil moisture," *IEEE Trans. Geosci. Remote Sens.*, vol. 28, no. 5, pp. 886–895, Sep. 1990. [Online]. Available: <https://ieeexplore.ieee.org/document/58978>
- [65] M. Zribi, O. Taconet, V. Ciarletti, and D. Vidal-Madjar, "Effect of row structures on radar microwave measurements over soil surface," *Int. J. Remote Sens.*, vol. 23, no. 24, pp. 5211–5224, Jan. 2002.
- [66] A. Marino, S. R. Cloude, and J. M. Lopez-Sanchez, "A new polarimetric change detector in radar imagery," *IEEE Trans. Geosci. Remote Sens.*, vol. 51, no. 5, pp. 2986–3000, May 2013.
- [67] A. Alonso-González, C. López-Martínez, K. P. Papathanassiou, and I. Hajnsek, "Polarimetric SAR time series change analysis over agricultural areas," *IEEE Trans. Geosci. Remote Sens.*, vol. 58, no. 10, pp. 7317–7330, Oct. 2020.
- [68] L. Zhu, J. P. Walker, N. Ye, and C. Rüdiger, "Roughness and vegetation change detection: A pre-processing for soil moisture retrieval from multi-temporal SAR imagery," *Remote Sens. Environ.*, vol. 225, pp. 93–106, May 2019.
- [69] L. Zhu, J. P. Walker, L. Tsang, H. Huang, N. Ye, and C. Rüdiger, "Soil moisture retrieval from time series multi-angular radar data using a dry down constraint," *Remote Sens. Environ.*, vol. 231, Sep. 2019, Art. no. 111237.
- [70] A. Ishimaru, T.-K. Chan, and Y. Kuga, "An imaging technique using confocal circular synthetic aperture radar," *IEEE Trans. Geosci. Remote Sens.*, vol. 36, no. 5, pp. 1524–1530, Sep. 1998. [Online]. Available: <https://ieeexplore.ieee.org/document/718856>
- [71] M. Pinheiro, P. Prats, R. Scheiber, M. Nannini, and A. Reigber, "Tomographic 3D reconstruction from airborne circular SAR," in *Proc. IEEE Int. Geosci. Remote Sens. Symp.*, Jul. 2009, pp. III-21–III-24. [Online]. Available: <https://ieeexplore.ieee.org/document/5418239>

- [72] M. Lort, A. Aguasca, C. López-Martínez, and T. M. Marín, "Initial evaluation of SAR capabilities in UAV multicopter platforms," *IEEE J. Sel. Topics Appl. Earth Observ. Remote Sens.*, vol. 11, no. 1, pp. 127–140, Jan. 2018.
- [73] V. Ignatenko, M. Nottingham, A. Radius, L. Lamentowski, and D. Muff, "ICEYE microsatellite SAR constellation status update: Long dwell spotlight and wide swath imaging modes," in *Proc. IEEE Int. Geosci. Remote Sens. Symp. (IGARSS)*, Jul. 2021, pp. 1493–1496.
- [74] R. Bindlish and A. P. Barros, "Multifrequency soil moisture inversion from SAR measurements with the use of IEM," *Remote Sens. Environ.*, vol. 71, no. 1, pp. 67–88, 2000.
- [75] X. Zhang, B. Chen, H. Fan, J. Huang, and H. Zhao, "The potential use of multi-band SAR data for soil moisture retrieval over bare agricultural areas: Hebei, China," *Remote Sens.*, vol. 8, no. 1, p. 7, 2015.
- [76] R. Guliaev, V. Cazcarra-Bes, M. Pardini, and K. Papatthanassiou, "Forest height estimation by means of TanDEM-X InSAR and waveform LiDAR data," *IEEE J. Sel. Topics Appl. Earth Observ. Remote Sens.*, vol. 14, pp. 3084–3094, 2021.
- [77] N. Romero-Puig and J. M. Lopez-Sanchez, "A review of crop height retrieval using InSAR strategies: Techniques and challenges," *IEEE J. Sel. Topics Appl. Earth Observ. Remote Sens.*, vol. 14, pp. 7911–7930, 2021.
- [78] N. Li et al., "Rice crop height inversion from TanDEM-X PolInSAR data using the RVoG model combined with the logistic growth equation," *Remote Sens.*, vol. 14, no. 20, p. 5109, Oct. 2022.
- [79] K. Belinska, G. Fischer, and I. Hajnsek, "Combining differential SAR interferometry and copolar phase differences for snow water equivalent estimation," *IEEE Geosci. Remote Sens. Lett.*, vol. 21, pp. 1–5, 2024.
- [80] A. Benedikter et al., "Toward dry snow parameter estimation by simultaneous multiple squint differential InSAR," *IEEE Trans. Geosci. Remote Sens.*, vol. 62, 2024, Art. no. 4303515. [Online]. Available: <https://ieeexplore.ieee.org/document/10735246>
- [81] Y. Yamaguchi, T. Moriyama, M. Ishido, and H. Yamada, "Four-component scattering model for polarimetric SAR image decomposition," *IEEE Trans. Geosci. Remote Sens.*, vol. 43, no. 8, pp. 1699–1706, Aug. 2005.
- [82] A. Passah, S. N. Sur, B. Paul, and D. Kandar, "SAR image classification: A comprehensive study and analysis," *IEEE Access*, vol. 10, pp. 20385–20399, 2022.
- [83] Y. Zhou, H. Wang, F. Xu, and Y.-Q. Jin, "Polarimetric SAR image classification using deep convolutional neural networks," *IEEE Geosci. Remote Sens. Lett.*, vol. 13, no. 12, pp. 1935–1939, Dec. 2016.
- [84] L. Huang, B. Jiang, S. Lv, Y. Liu, and Y. Fu, "Deep-learning-based semantic segmentation of remote sensing images: A survey," *IEEE J. Sel. Topics Appl. Earth Observ. Remote Sens.*, vol. 17, pp. 8370–8396, 2024.
- [85] C. Liu et al., "A review of optical and SAR image deep feature fusion in semantic segmentation," *IEEE J. Sel. Topics Appl. Earth Observ. Remote Sens.*, vol. 17, pp. 12910–12930, 2024.
- [86] N. Li, D. Xiang, H. Ding, Y. Xie, and Y. Su, "Edge-constrained temporal superpixel segmentation and graph-structured energy optimization for PolSAR change detection," *ISPRS J. Photogramm. Remote Sens.*, vol. 229, pp. 49–64, Nov. 2025.
- [87] D. A. Morgan, "Deep convolutional neural networks for ATR from SAR imagery," *Proc. SPIE*, vol. 9475, pp. 116–128, May 2015.
- [88] D. Xiang, Y. Lu, D. Guan, G. Li, J. Cheng, and B. Li, "Oil spill detection in PolSAR imagery using composite scattering power entropy and multiscale hybrid feature fusion network," *IEEE J. Sel. Topics Appl. Earth Observ. Remote Sens.*, vol. 18, pp. 13388–13407, 2025.



Nikita Basargin (Graduate Student Member, IEEE) received the B.Sc. and M.Sc. degrees in computer science from the Technical University of Munich (TUM), Munich, Germany, in 2017 and 2020, respectively. He is currently pursuing the Ph.D. degree in cooperation with Munich School for Data Science (MUDS) and the TUM School of Life Sciences, TUM, Freising, Germany.

Since 2021, he has been with the Microwaves and Radar Institute, German Aerospace Center (DLR), Weßling, Germany. His research interests include the

application of data science and machine learning methods to remote sensing SAR data, visualization, optimization, and biophysical information retrieval.

Mr. Basargin was a member of the Max Weber Program from 2014 to 2020. He was a recipient of the Rohde & Schwarz Best Bachelor Award in 2017 and the IEEE GRSS IADF School Best Poster Award in 2023.



Alberto Alonso-González received the B.Sc. degree in computer science and the M.Sc. and Ph.D. degrees in telecommunication engineering from the Technical University of Catalonia (UPC), Barcelona, Spain, in 2007, 2009, and 2014, respectively.

From 2009 to 2014, he was with the Department of Signal Theory and Communications, UPC. From 2014 to 2022, he was with the Microwaves and Radar Institute, German Aerospace Center (DLR), Weßling, Germany, as a member of the Polarimetric SAR Interferometry Research Group. Since 2022, he has been with the CommSensLab Group, Department of Signal Theory and Communications, UPC. His research interests include multidimensional synthetic aperture radar (SAR), SAR polarimetry and interferometry, and digital signal and image processing. His research activities are focused on remote sensing data modeling and machine learning techniques applied to agricultural and forest monitoring for climate change mitigation.

Dr. Alonso-González was a recipient of the First Place Student Paper Award from the EUSAR 2012 Conference and the Extraordinary Doctoral Thesis Award from the Technical University of Catalonia in 2016.



Irena Hajnsek (Fellow, IEEE) received the Dipl. degree (Hons.) in the topic of fluvial river systems from the Free University of Berlin, Berlin, Germany, in 1996, the Dr. rer. nat. degree (Hons.) in model-based estimation of soil moisture from fully polarimetric synthetic aperture radar from Friedrich Schiller University Jena, Jena, Germany, in 2001, and the Doctor Honoris Causa degree from the University of Oslo, Oslo, Norway, in 2024, for her outstanding contributions to science, including the development of algorithms using innovative radar

techniques for environmental parameter estimation and setting requirements for the design of future radar missions in application areas as permafrost, glaciers, disaster management, agriculture, and climate change impacts.

Since November 2009, she has been a Professor of Earth observation with the Institute of Environmental Engineering, Swiss Federal Institute of Technology (ETH) Zürich, Zürich, Switzerland, and the Head of the Polarimetric SAR Interferometry Research Group, Microwaves and Radar Institute, German Aerospace Center, Weßling, Germany. Since 2010, she has been the Science Coordinator of the German satellite mission TanDEM-X. Her main research interests include electromagnetic propagation and scattering theory, radar polarimetry, SAR and interferometric SAR data processing techniques, and environmental parameter modeling and estimation.

Dr. Hajnsek is a member of the European Space Agency Mission Advisory Group for the ROSE-L Mission. From 2013 to 2021, she was a member of the IEEE GRSS AdCom. She was the Technical Program Co-Chair of the IEEE IGARSS 2012 in Munich, Germany, and the IEEE IGARSS 2019 in Yokohama, Japan. From 2016 to 2020, she was the Vice President of the IEEE GRSS Technical Committees. She is the Founder in 2021 and was the Chair (2021–2025) of the new Technical Committee Remote sensing Environment, Analysis and Climate Technologies (REACT).